Journal of Materials Chemistry B

ROYAL SOCIETY OF CHEMISTRY

PAPER

View Article Online
View Journal

Cite this: DOI: 10.1039/d5tb00860c

Innovative diopside–$MnFe_2O_4$ nanocomposites: a multifunctional platform for bone regeneration and hyperthermia therapy featuring $MnFe_2O_4$ nanoparticles with near-bulk magnetic performance

Guan-Xiang Liao,†[a] Wei-Hsi Chang,†[abc] Yu-Sheng Tseng†[a] and Wen-Fan Chen *[a]

This study explores the novel integration of $MnFe_2O_4$ nanoparticles into diopside bioceramics, paving the way for advanced multifunctional nanocomposites tailored for orthopedic and oncological applications. Diopside is synthesized using biowaste-derived eggshells and rice husks *via* solid-state reaction at an optimal sintering temperature of 1200 °C. $MnFe_2O_4$ nanoparticles, with an average particle size of 46 nm, are produced through a facile hydrothermal method coupled with magnetic separation, achieving an impressive saturation magnetization (M_s) of 81.6 emu g^{-1} (99.5% of bulk $MnFe_2O_4$) – the highest reported to date. This exceptional performance is attributed to the nanoparticles' excellent crystallinity, single-domain behavior, and minimized surface effects. Incorporating $MnFe_2O_4$ nanoparticles into diopside significantly enhances the sinterability, density, and hardness by 2–2.5 times while reducing porosity to ~1%. Even at a low addition of 10 wt% $MnFe_2O_4$, the nanocomposites demonstrate effective hyperthermia within a safe therapeutic range (41–46 °C) under an alternating magnetic field, with negligible coercivity and remanence. Biocompatibility evaluations confirm no cytotoxicity and reveal enhanced osteoblast differentiation and mineralization. This study successfully synthesizes $MnFe_2O_4$ nanoparticles with near-bulk saturation magnetization and highlights diopside–$MnFe_2O_4$ nanocomposites as promising candidates for sustainable and multifunctional biomaterials, offering load-bearing support, efficient hyperthermia for osteosarcoma therapy, and accelerated bone regeneration.

Received 12th April 2025,
Accepted 28th July 2025

DOI: 10.1039/d5tb00860c

rsc.li/materials-b

1. Introduction

Osteosarcoma is a highly aggressive bone tumor,[1,2] characterized by significant metastatic potential, frequent recurrence, and poor prognosis,[3] even leading to severe pathological fractures.[4] It is most commonly diagnosed in adolescents and young adults, typically between the ages of 10 and 25.[5] This malignant tumor frequently occurs in the distal femur, proximal tibia, proximal humerus, and proximal femur,[6,7] which are key joints crucial for daily activities and mobility. The treatment of osteosarcoma and other malignant bone tumors presents substantial challenges in orthopedic surgery because clinical preference often leans toward limb preservation after tumor removal, instead of amputation. This approach requires not only the complete removal of the tumors but also the subsequent reconstruction of the resulting bone defects. Despite significant advances in biomedical science, effective cancer treatment remains less than satisfactory. Traditional approaches such as surgical resection, chemotherapy, radiation therapy, and drug therapy have improved patient survival rates but often come with undesirable side effects, such as hair loss, nausea, and damage to healthy tissues.[8] Incomplete removal of tumor cells also increases the likelihood of recurrence and metastasis, even after functional recovery and limb salvage.[1,2,7] Furthermore, the extensive bone damage caused by tumor resection may exceed the bone's natural regenerative capacity.[9] Therefore, it is crucial to develop bioactive materials that not only provide sufficient capability for bone regeneration and repair post-resection but also effectively eliminate residual tumor cells, ensuring successful bone reconstruction and restoration of normal function.

Bioactive ceramic materials, particularly calcium phosphate and calcium silicate, have become dominant in the field of

[a] *Institute of Medical Science and Technology, National Sun Yat-sen University, Kaohsiung 80424, Taiwan. E-mail: sallychen@imst.nsysu.edu.tw*
[b] *Department of Emergency Medicine, Kaohsiung Armed Forces General Hospital, Kaohsiung 80284, Taiwan*
[c] *Department of Emergency Medicine, Tri-Service General Hospital, National Defense Medical Center, Taipei 11490, Taiwan*
† These authors contributed equally.

orthopedic applications.[10–14] Hydroxyapatite (HAp), a calcium phosphate-based ceramic that closely mimics the mineral composition of human bone, is widely used in clinical settings as an artificial bone graft due to its exceptional biocompatibility for bone tissue repair.[15] Although HAp is known for its excellent ability to promote bone regeneration, its low mechanical strength limits its suitability for load-bearing orthopedic applications.[16] In contrast, calcium silicate bioceramics, including compositions like Ca–Si–X (X = Mg, Zn, Zr, *etc.*), are emerging as promising alternatives.[17] The release of specific concentrations of calcium and silicon ions from these materials has been shown to promote osteoblast proliferation and differentiation, processes critical for effective bone regeneration.[17–19] Moreover, the chemical versatility of calcium silicate-based bioceramics allows for the tuning of its mechanical properties, making it more suitable for load-bearing applications.[20] Among calcium silicate bioceramics, diopside ($CaMgSi_2O_6$) stands out due to its superior compressive strength, mechanical properties, and controllable degradation rate.[11] Magnesium ions (Mg^{2+}), naturally abundant in the human body, not only enhance cell growth and differentiation but also improve the biocompatibility of bioceramics.[21,22] Studies suggest that Mg^{2+} ions regulate the early-stage decomposition of calcium and phosphate, resulting in reduced degradation in simulated body fluid (SBF) environments.[14] Furthermore, the higher bonding energy of Mg–O compared to Ca–O provides greater stability to the crystal structure, further enhancing the material's durability and performance.[14,23,24]

There are various methods to synthesize diopside, including sol–gel,[25] co-precipitation,[26–28] melt-quenching,[29] and solid-state reaction.[11–13,30] Among these, the solid-state reaction is the most widely used due to its simplicity, cost-effectiveness, and easy accessibility of raw materials. In this study, calcium oxide (CaO) derived from eggshells serves as the calcium source, while silica (SiO_2) extracted from rice husks provides the silicon source. The goal is to recycle agro-industrial wastes into bioceramics for bone defect repair. Agro-industrial wastes refer to materials generated during the cultivation and processing of vegetables, poultry, meat, fruits, crops, and dairy products.[31] In the European Union, 118–138 million tons of bio-waste are generated annually, of which only 25% is recycled into high-quality compost or digestate. The remainder is disposed of through landfilling, which leads to the emission of large amounts of greenhouse gases.[32] According to the Food and Agriculture Organization of the United Nations (FAO), global egg production reached 93 million tons in 2022.[33] Since eggshells account for about 11% of the total dry weight of an egg,[34] this results in approximately 8 million tons of bio-waste annually, with only a small fraction being used as natural fertilizer. Eggshells consist of 94% calcium carbonate, 1% calcium phosphate, 1% magnesium carbonate, and 4% organic matter, making them a viable calcium source for bioceramic production.[12,35,36] Calcium is a crucial component in bioceramics, which is why research on using waste eggshells as a calcium source has also been applied to calcium silicate bioceramics.[11,13,14] Moreover, rice is a staple food for much of the world, and rice husks, which make up 20–30% of the total weight of harvested rice,[37] are a major byproduct. Studies have shown that rice husks, when pre-treated with acid, can yield up to 99% silica,[11,38,39] making them an ideal silicon source. Calcium silicate bioceramics synthesized using rice husk-derived silica demonstrate excellent apatite-forming ability, cell compatibility, and osteoblast proliferation-stimulating effects.[11,13]

Another focus of this study is how to eliminate residual tumor cells in bone defects following surgery. Thermotherapy is gaining attention as an alternative physical treatment for tumors.[40,41] By elevating the temperature to 41–46 °C, thermotherapy can effectively destroy tumor cells while sparing healthy tissues.[42,43] Research has shown that a few minutes of sustained heating at the treatment site can be effective, as tumor cells are more sensitive to temperature fluctuations than normal cells.[44–46] Among various thermotherapy techniques, magnetic nanoparticles are widely used in magnetothermal therapy due to their unique physical properties and excellent biocompatibility.[44–59] When exposed to an alternating magnetic field, these nanoparticles generate heat through Néel and Brownian relaxation, as well as hysteresis loss,[44,45,49,51,58,59] leading to the destruction of tumor cells. Recent studies have also suggested that localized heating may not only ablate tumors but also stimulate beneficial biological responses such as enhanced cell proliferation and osteogenic differentiation, potentially aiding tissue regeneration processes.[60,61] Although many magnetic materials have been investigated for their heating potential, the focus of most studies has been on magnetic iron oxides, such as Fe_3O_4 (magnetite) and γ-Fe_2O_3 (maghemite).[44,45,47,50,56] While these materials are well tolerated by the human body, $MnFe_2O_4$ (manganese ferrite) offers even higher biocompatibility,[62] positioning it as a promising candidate for biomedical applications, including drug delivery,[63] magnetic resonance imaging (MRI),[64] magnetic hyperthermia therapy,[51,55] and enzyme-mimetic catalysis such as peroxidase-like and oxidase-like activity.[65] In environmental catalysis, $MnFe_2O_4$ has been used as an efficient magnetically-responsive catalyst for pollutant degradation due to its redox-active Mn^{2+}/Fe^{3+} ions. In a recent study, $MnFe_2O_4$@BCZT core–shell nanostructures generated reactive oxygen species (ROS) under an alternating magnetic field *via* magnetoelectric coupling, enabling highly effective degradation of Rhodamine B without added chemical agents.[66]

Moreover, due to its superparamagnetic properties, $MnFe_2O_4$ nanoparticles are considered an ideal heat source for cancer treatment through magnetothermal therapy under an alternating magnetic field. Once the magnetic field is removed, the magnetization of these particles disappears, which helps prevent particle aggregation. The heating efficiency of $MnFe_2O_4$ nanoparticles in such a field is closely related to their saturation magnetization (M_s), which is influenced by factors such as particle size, shape, and the cation distribution within the tetrahedral and octahedral sites of the mixed spinel structure.[62] Theoretically, the maximum saturation magnetization for bulk $MnFe_2O_4$ can reach approximately 80–82 emu g^{-1} at room temperature,[67,68] whereas experimental values for nanoparticles typically range from 30 to 76 emu g^{-1} depending on the synthesis method and crystallinity.[62]

Compared with Fe_3O_4, which has a theoretical M_s of 92 emu g^{-1},[69] $MnFe_2O_4$ shows a slightly lower saturation magnetization, but it offers greater chemical stability, higher resistance to oxidation, and more favorable cation substitution flexibility, making it more tunable for biomedical applications.[67] In addition, $MnFe_2O_4$ shows enhanced heating efficiency at lower doses due to its tailored magnetic anisotropy and spin structure,[70] indicating that it can achieve comparable or even superior hyperthermia performance under clinical AC magnetic field conditions.

Given this context, it is imperative to develop a multifunctional biomaterial capable of both eliminating residual bone tumor cells and repairing bone defects while providing mechanical support during the bone healing process. $MnFe_2O_4$ was selected as the magnetic nanoparticle for hyperthermia therapy in this study due to its excellent heating efficiency and the beneficial effects of Mn^{2+} and Fe^{2+}/Fe^{3+} ions on bone regeneration.[71,72] Specifically, Mn^{2+} ions have been shown to promote osteogenic differentiation by activating the extracellular signal-regulated kinases (ERK1/2) pathway, leading to the upregulation of osteoblast-related genes such as RUNX2, ALP, OCN, and OPN in mesenchymal stem cells.[73] Fe^{2+}/Fe^{3+} ions also enhance osteoblast proliferation and differentiation by reducing intracellular hydrogen peroxide levels through intrinsic peroxidase-like activity and by accelerating cell cycle progression *via* the regulation of key cell cycle proteins, including cyclins and CDKs.[74] The synergistic effect of Mn^{2+} and Fe ions not only stimulates early-stage osteogenic activity but also helps modulate local redox balance and maintain the structural integrity of the extracellular matrix. This dual functionality provides a valuable platform for bone tissue engineering, particularly in post-tumor resection scenarios where both regeneration and residual tumor ablation are required.

In the current literature, the incorporation of $MnFe_2O_4$ into bioactive glass-ceramics is more prevalent compared to its combination with other types of bioceramics.[71,72,75–78] Li *et al.*[72] developed a magnetic bioactive glass ceramic in the $CaO–SiO_2–P_2O_5–MgO–CaF_2–MnO_2–Fe_2O_3$ system, composed of $CaSiO_3$ and $Ca_5(PO_4)_3F$ as the primary phases, with $MnFe_2O_4$ and Fe_3O_4 contributing the magnetic properties. It exhibited a saturation magnetization of 6.4 emu g^{-1}, promoted hydroxyapatite formation after 14 days in SBF, and supported successful cell attachment and proliferation. Tripathi *et al.*[77] investigated strontium bioactive glass ($46.1SiO_2–21.9CaO–24.4Na_2O–2.6P_2O_5–5SrO$) and manganese ferrite ($MnFe_2O_4$) composites, demonstrating biocompatibility with MG-63 cells, antibacterial activity against *E. coli* and *S. aureus*, and superparamagnetic behavior at room temperature with heating potential, confirming their suitability for hyperthermia applications. Oskoui *et al.*[78] studied the effect of adding varying MnO_2 wt% to $20SiO_2–50FeO–15CaO–15Na_2O$ glass-ceramics, which led to the crystallization of γ-Fe_2O_3, α-Fe_2O_3, $MnFe_2O_4$, and Na_2CaSiO_4 phases. Increasing MnO_2 content from 0 to 15 wt% enhanced the saturation magnetization from 21.5 emu g^{-1} to 30.8 emu g^{-1}, and hydroxyapatite with a cauliflower-like morphology was observed after immersion in simulated body fluid. Additionally, in a few studies, $MnFe_2O_4$ has been combined with hydroxyapatite for applications aimed at treating bone cancer.[79–81] Pon-On *et al.*[80] investigated the substitution of iron and manganese into hydroxyapatite, yielding ceramics with the empirical formula $Ca_{9.4}Fe_{0.4}Mn_{0.2}(PO_4)_6(OH)_2$. TEM images revealed a core/shell structure in the nano-$MnFe_2O_4$ hydroxyapatite particles, where the ferrite core crystallized from the Fe/Mn substitution in hydroxyapatite upon heating above 500 °C, surrounded by a hydroxyapatite shell. Arabzadeh *et al.*[81] explored the use of quercetin (QC), a natural anticancer agent, to assess the performance of mesoporous magnetic $MnFe_2O_4$ core–shell nanocomposites. The $MnFe_2O_4$ core was synthesized *via* a co-precipitation method and coated with a mesoporous hydroxyapatite shell for drug loading. Compared to free QC, the loaded QC demonstrated higher antioxidant activity and enhanced anticancer efficacy.

In this study, diopside ($CaMgSi_2O_6$) was selected as the base bioceramic due to its ability to provide essential load-bearing support, which is crucial for maintaining mechanical integrity while facilitating the repair of bone defects. It was synthesized using biowaste materials – rice husk (as a silica source[11,13,38,39]) and eggshells (as a calcium source[11–14,35,36,82,83]) – and incorporated with varying proportions of $MnFe_2O_4$ nanoparticles (10/20/30 wt%) as a heat generator for hyperthermia treatment of bone tumors. Notably, the incorporation of $MnFe_2O_4$ magnetic nanoparticles into diopside has not been previously explored in the literature. This study investigates the effects of the diopside–$MnFe_2O_4$ nanocomposites on mineralogy, morphology, mechanical properties, cell biocompatibility, alkaline phosphatase (ALP) activity, and ARS staining. Additionally, the *in vitro* magnetic hyperthermia potential is evaluated. Although this study focuses on *in vitro* characterization and cellular responses, further *in vivo* studies will be essential to evaluate long-term biocompatibility, metal ion biodistribution, and the therapeutic efficacy of the nanocomposites in bone regeneration and tumor ablation.

2. Materials and methods

2.1 Materials

To obtain SiO_2 powder, rice husks were first cleaned with RO (reverse osmosis) water to remove dirt and dust. They were then immersed in 0.5 M diluted hydrochloric acid and stirred at 60 °C for 30 min. Afterward, the rice husks were thoroughly rinsed with deionized (DI) water to remove any residual acid and dried in an oven at 110 °C overnight. The dried husks were subsequently calcined in a furnace at 700 °C for 6 h, with a heating rate of 10 °C min^{-1}, and allowed to cool naturally to room temperature, resulting in white rice husk ash (SiO_2 powder). For CaO powder preparation, eggshells were boiled at 100 °C to remove membrane proteins, then rinsed five times with DI water and dried in an oven at 120 °C for 2 h. The dried eggshells were ground into a fine powder and calcined in a furnace at 900 °C for 2 h, with a heating rate of 5 °C min^{-1}. After cooling to room temperature, the powder was sieved to a particle size of 200 μm to obtain white CaO powder.

To synthesize magnetic nanoparticles, ferric chloride hexahydrate ($FeCl_3·6H_2O$, 97%, Duksan, Korea) and manganese

chloride tetrahydrate ($MnCl_2{\cdot}4H_2O$, Sigma-Aldrich, USA) were dissolved in 70 mL of DI water at a molar ratio of 2 : 1 and stirred magnetically for 30 min until fully dissolved. Next, 5 M NaOH was titrated slowly until substantial dark brown precipitates formed, followed by continuous stirring for 1 h. The resulting solution was transferred to a 100 mL Teflon-lined hydrothermal autoclave, which was then sealed and heated in an oven at 200 °C for 12 h. After cooling to room temperature, the precipitates were washed multiple times with DI water and ethanol using a neodymium magnet (2700 Oe) for magnetic separation to ensure the complete removal of impurities. The final product was dried in an oven at 70 °C for 24 h to obtain pure black $MnFe_2O_4$ nanoparticles.

2.2 Preparation of diopside–$MnFe_2O_4$ nanocomposites

Firstly, eggshell powder (CaO), magnesium oxide (MgO, 99%, UniRegion Bio-Tech, Taiwan), and rice husk ash (SiO_2) were weighed in a molar ratio of 1 : 1 : 2, and ball-milled at 400 rpm for 6 h using a planetary ball mill (BM6pro, POWTEQ, China) with a ball-to-powder ratio of 10 : 1. The resulting mixed powder was then sieved to a particle size of 200 μm. A total of 0.3 g of mixture (diopside precursor) was loaded into a compressing mold, and 2 wt% of sunflower oil was added as a binder, followed by uniaxial pressing at 150 MPa for 30 s to form a dense round pellet (∅13 × H1.8 mm). Pure diopside was obtained by sintering the pellet in air at 1200 °C for 3 h, with a heating rate of 5 °C min^{-1}, followed by natural cooling to room temperature. To synthesize diopside–$MnFe_2O_4$ nanocomposites, a procedure similar to that of pure diopside synthesis was performed, with $MnFe_2O_4$ magnetic nanoparticles added to the diopside precursor in proportions of 10, 20, and 30 wt%. The resulting nanocomposites were labeled as Di–*X*MnFe (*X* = 0, 10, 20, and 30), according to the $MnFe_2O_4$ content. Fig. 1 illustrates the preparation process of the diopside–$MnFe_2O_4$ nanocomposites.

2.3 Characterization

Mineralogical properties were analyzed using a powder X-ray diffractometer (D2 Phaser, Bruker, USA) with Cu Kα radiation (λ = 1.54184 Å) at 30 kV and 10 mA, over a diffraction angle range (2θ) from 10° to 70°, with a step size of 0.01° 2θ. The diffraction patterns were processed and phase identification was carried out using Match! software (Crystal Impact, Germany). Quantitative phase analysis was performed using the Rietveld refinement method *via* FullProf Suite integrated with Match! software. Thermal stability, phase transformation, and crystallization temperature were assessed *via* thermogravimetric/differential scanning calorimetry (TGA/DSC, Mettler-Toledo, 2-HT, Switzerland) under a nitrogen environment, with a heating rate of 5 °C min^{-1} from 30 °C to 1000 °C. Surface morphology and quantitative chemical composition were examined using a field emission electron probe microanalyzer (FE-EPMA, JXA-8530F, JEOL, Japan), equipped with a scanning electron microscope (SEM) and a wavelength dispersive spectrometer (WDS). The FE-EPMA operated at 15 kV with an analytical depth of approximately 700 nm. Backscattered electron imaging was employed to distinguish between different compounds, while the WDS point mode was used for precise determination of elemental concentrations. The morphology and particle size distribution of the magnetic $MnFe_2O_4$ nanoparticles were characterized using transmission electron microscopy (TEM, Hitachi H7100, Japan). Magnetic properties were investigated using a superconducting quantum interference device (SQUID, Quantum Design, USA), with hysteresis curves generated by varying the magnetic field (H) between −5000 Oe and +5000 Oe at 300 K. Vickers hardness was measured using a

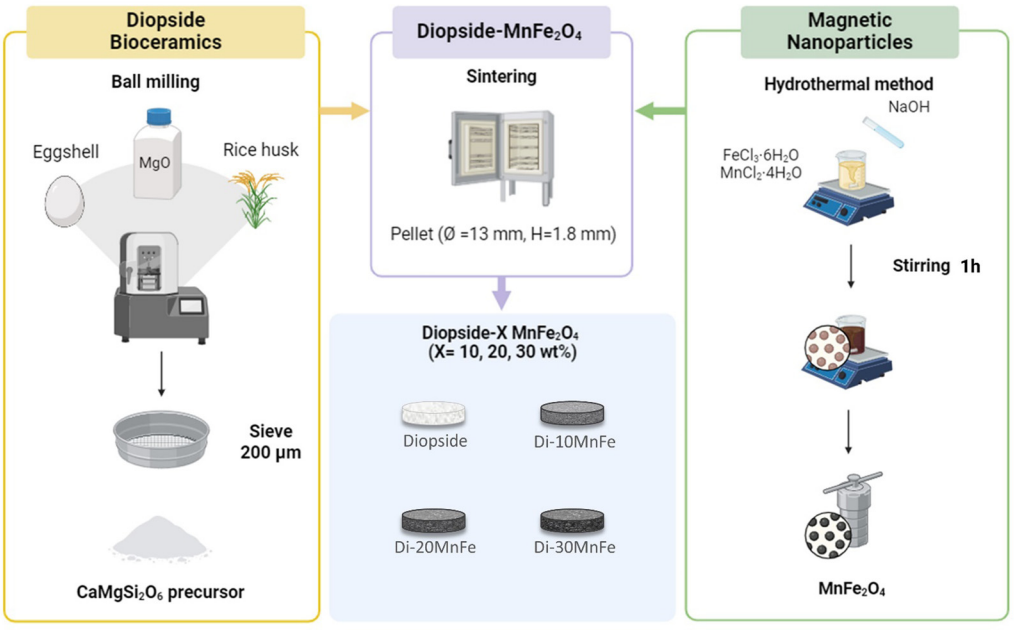

Fig. 1 Flow chart of diopside–$MnFe_2O_4$ nanocomposite preparation.

Vickers hardness tester (FM-810, Future-Tech, Japan) with an applied load of 1 kg and a dwell time of 10 s.

The bulk and apparent densities, as well as the porosity, of sintered pure diopside and diopside–$MnFe_2O_4$ nanocomposites were determined in DI water using the Archimedes method. Firstly, the samples were dried in an oven at 110 °C overnight to eliminate any moisture, and then allowed to cool to room temperature in a moisture-proof container without humidity for 24 h. The dry weight of each sample, denoted as m_1, was measured with a high-precision analytical balance (AS 220.R2 PLUS, Radwag, Poland) with an accuracy of 1 mg. The samples were then saturated with DI water by vacuum for 2 h, after which their immersed mass, m_2, was recorded while suspended in DI water. After removing the samples from the water and carefully wiping off excess surface moisture, their saturated weight in air, m_3, was measured. The following equations were used for the calculations, where ρ_0 represents the density of DI water at 25 °C.

$$\text{Bulk density } (D_B) = (m_1 \times \rho_0)/(m_3 - m_2) \quad (1)$$

$$\text{Apparent density } (D_A) = (m_1 \times \rho_0)/(m_1 - m_2) \quad (2)$$

$$\text{Porosity } (\%) = \left[1 - \left(\frac{D_B}{D_A}\right)\right] \times 100\% \quad (3)$$

2.4 Magnetic hyperthermia properties *in vitro*

To assess the magnetic hyperthermia properties of the diopside–$MnFe_2O_4$ nanocomposites, an inductive heating device (ANG-06A-I, Aneng, Taiwan) was employed. A 20 mg sample of sintered nanocomposite was placed in an open vial containing 1 g of water, and the vial was positioned at the center of an alternating magnetic field coil, operating at a frequency of 287 KHz with a fixed field amplitude of 30 Oe. During the application of the alternating magnetic field, temperature data was recorded every second using a fiber-optic thermometer (H201, Rugged Monitoring, Canada). The heat generated by the magnetic nanoparticles under the influence of the alternating magnetic field caused a rise in the sample's temperature. The relationship between heat and temperature was described by the following equation:

$$\Delta Q = m_{water}C_{water}\Delta T + m_{sample}C_{sample}\Delta T \quad (4)$$

where m_{water} represents the mass of water (1 g), m_{sample} is the mass of the sample (20 mg), C_{water} is the specific heat capacity of water (4.185 J g^{-1} K^{-1}), C_{sample} is the specific heat capacity of the sample, and ΔT is the change in temperature (K) of the sample.

Specific loss power (SLP) is defined as the amount of heat dissipated per unit mass of magnetic nanoparticles (W g^{-1}). In this study, the initial slope method was employed to evaluate the heating efficiency of the sample under an alternating magnetic field. The SLP was calculated by the following eqn (5) in combination with the eqn (4):

$$\text{SLP} = \frac{\frac{\Delta Q}{\Delta t}}{m_{sample}} = \frac{\frac{\Delta T}{\Delta t}}{m_{sample}}\left[m_{water}C_{water} + m_{sample}C_{sample}\right] \cong \frac{m_{water}C_{water}}{m_{sample}}\left(\frac{\Delta T}{\Delta t}\right) \quad (5)$$

where $\Delta T/\Delta t$ represents the initial slope of the temperature change over time (second).

2.5 Cell culture of the MC3T3-E1 cell line

MC3T3-E1 cells (ATCC-CRL-2593, USA), derived from mice, were cultured in Alpha Minimal Essential Medium (Alpha-MEM, Gibco, USA) supplemented with 10% fetal bovine serum (FBS, Sigma-Aldrich, USA) and 0.5% penicillin–streptomycin (Sigma-Aldrich, USA). The cells were maintained at 37 °C in a humidified atmosphere with 5% CO_2.

2.6 Cell viability and proliferation

Cell viability was assessed using liquid extracts from the nanocomposite samples through an MTT assay (3-(4,5-dimethylthiazol-2-yl)-2,5-diphenyltetrazolium bromide, 98%, Alfa Aesar, USA). MTT was dissolved in sterile and filtered phosphate-buffered saline (PBS) to a concentration of 5 mg mL^{-1}. The positive control group contained SDS (99%, JT Baker, USA), while the negative controls included a cell-only group and a group treated with alumina (Al_2O_3, 99.5%, Sigma-Aldrich, USA).

MC3T3-E1 cells were seeded into 96-well plates at a density of 2×10^3 cells per well and cultured in 100 μL of Alpha-MEM in a humidified incubator at 37 °C with 5% CO_2 for 24 h. Liquid extracts from all test groups were prepared by immersing the nanocomposite materials in Alpha-MEM at a concentration of 0.2 g mL^{-1} (0.2 mg mL^{-1} for the SDS group) at 37 °C for 24 h, followed by filtration through a 0.22 μm filter. After 24 h of incubation, the Alpha-MEM was removed, and 100 μL of the filtered extract was added to each well. MC3T3-E1 cells were incubated in these extracts for 24 h to assess cytotoxicity. Then, 10 μL of the MTT solution (5 mg mL^{-1} in PBS) was added to each well and incubated for 2 h at 37 °C in 5% CO_2. After incubation, the MTT solution was discarded, and 100 μL of dimethyl sulfoxide (DMSO, 99.5%, Sigma-Aldrich, USA) was added to each well to dissolve the purple formazan crystals. Absorbance at 570 nm was measured using an ELISA microplate reader (Eon, BioTek, USA), and cell viability was calculated by the following equation:

$$\text{Cell viability } (\%) = (OD_s \div OD_c) \times 100\% \quad (6)$$

where OD_s is the absorbance of the sample, and OD_c is the absorbance of the control group containing only cells. Quantitative data are presented as the mean ± standard deviation from six replicates per experiment.

The effect of different nanocomposite samples on the proliferation of MC3T3-E1 cells was further investigated by seeding the cells into 96-well tissue culture plates at an initial density of 2×10^3 cells per well in standard Alpha-MEM. After 24 h of incubation, the culture medium was replaced with 100 μL of material extracts supplemented with 10% FBS, while 100 μL of standard Alpha-MEM containing 10% FBS served as a blank control. On days 1, 3 and 7, cell proliferation of MC3T3-E1 cultured in the material extracts was assessed using the MTT assay.

2.7 Alkaline phosphatase assay (ALP)

Alkaline phosphatase assay (ALP) is a key early marker of osteogenic differentiation, as its activity reflects the maturation of osteoblasts and the mineralization process. Firstly, MC3T3-E1 cells were seeded at a density of 2×10^4 cells per well in a 24-well plate and cultured in an incubator at 37 °C with 5% CO_2 for three days, allowing the cells to adhere and reach 80% confluency. The test extracts were prepared by immersing nanocomposite materials in an osteogenic induction medium (OIM) containing 50 μg mL^{-1} L-ascorbic acid, 10 mM β-glycerophosphate, and 100 nM dexamethasone, at a concentration of 0.2 g mL^{-1}. On the third day of incubation, the osteogenic induction extracts were collected and filtered through a 0.22 μm syringe filter. The filtered extracts were added to the 24-well plate at 400 μL per well, while the control group received fresh OIM. Both the extracts and OIM were replaced every two days, and ALP analysis was conducted on days 7 and 14.

For ALP analysis, the culture medium was firstly removed, and the cells were washed with PBS. Then, 400 μL of 4% paraformaldehyde was added to each well and incubated for 10 min. After removing the paraformaldehyde, the wells were rinsed with DI water. BCIP/NBT color reagent (Revvity, USA) was then added to each well (450 μL per well) and incubated for 45 min, resulting in dark purple staining at the phosphatase-active sites. The intensity of this staining correlates with ALP activity, indicating the level of osteogenic differentiation. To quantify ALP activity, the stained cells were observed using an optical microscope (IX73P1F, Olympus, Japan), and ImageJ software was used for quantitative analysis.

2.8 Alizarin Red S mineralization assay (ARS)

Alizarin Red S assay (ARS) is used to assess calcium mineralization, a critical marker of late-stage osteogenic differentiation. By detecting and quantifying calcium deposition in the extracellular matrix, this assay provides a reliable measure of the extent of mineralization, reflecting the maturity of the bone-like tissue formed by the cells.

For ARS analysis, the preparation and addition of osteogenic induction extracts, as well as cell culture, were performed in the same way as for the ALP assay. The primary difference in the ARS assay is that it was conducted after 21 days of cell culture. At this point, the osteogenic induction extracts were removed, and the cells were washed with PBS. Next, 400 μL of 4% paraformaldehyde was added to each well and incubated for 10 min to fix the cells. After removing the paraformaldehyde, the residual liquid was rinsed off with DI water. Then, 420 μL of 2% alizarin red S solution (pH 4.2, Alfa Aesar, USA) was added to each well and incubated for 45 min to allow for calcium staining. Calcium deposition, indicative of mineralization, appeared as an orange-red color. The alizarin stain was subsequently dissolved with 10% acetic acid, and the absorbance at 450 nm was measured to quantify the staining intensity.

2.9 Statistical analysis

All data were presented as the mean ± standard deviation (SD). Statistical analysis was performed using one-way analysis of variance (ANOVA) followed by Tukey's *post hoc* test in GraphPad Prism. A *p*-value of less than 0.05 was considered statistically significant.

3. Results and discussion

3.1 Characterization of diopside bioceramics

The XRD patterns of rice husk and eggshell after calcination are shown in Fig. 2(a) and (b). Raw rice husk contains approximately 15–23% silica, with the remaining portion consisting of organic matter (cellulose, hemicellulose, lignin). The decomposition of rice husk into ash occurs in three stages: (1) moisture loss, (2) decomposition of the organic fraction, leading to the elimination of volatile organic compounds (VOCs), and (3) carbon removal. As a result, heat treatment can increase the silica purity to as much as 95%,[38] while acid treatment of rice husks prior to sintering yields silica with a purity exceeding 99%.[39] This is confirmed in Fig. 2(a), where rice husk treated with acid followed by calcination resulted in amorphous silica. As for raw eggshells, which make up 11% of the total weight of an egg, they are composed of 94% calcium carbonate, 1% calcium phosphate, 1% magnesium carbonate, and 4% organic matter.[36] Fig. 2(b) shows that pure calcium oxide (CaO) was obtained after the heat treatment of eggshell powder, which aligns with the standard reference of CaO (ICSD code: 51409).

The thermal stability and phase transformation of the ball-milled diopside precursor were investigated using TGA and DSC. As depicted in Fig. 2(c), the TGA curve reveals three primary stages of weight loss. The first stage, with a minor weight loss of approximately 0.4% below 150 °C, corresponds to the removal of residual moisture.[11,84] The second stage shows a significant endothermic peak around 393 °C, with a weight loss of about 2.7%, which is attributed to the dehydration of chemically adsorbed water, as CaO in the precursor readily absorbs moisture from the environment, forming calcium hydroxide.[85,86] The final weight loss, approximately 1.4%, occurs between 450 °C and 1000 °C and is likely due to the decarburization of incompletely condensed by-products. The constant mass beyond 800 °C indicates that no further decomposition occurred. In the DSC curve, an exothermic peak is observed around 845 °C, which corresponds to the crystallization temperature of diopside. This result is consistent with previous studies on diopside synthesis using different starting materials.[13,14,87,88]

Based on the TGA/DSC analysis shown in Fig. 2(c), the sintering temperature for diopside in this study was set at 900–1200 °C. The optimum sintering temperature was further evaluated by analyzing the crystallization temperature of diopside obtained from TGA/DSC, with the corresponding XRD results shown in Fig. 2(d). When the precursor powders were sintered at 900 °C for 3 h, the formation of the major phase (diopside, $CaMgSi_2O_6$) along with secondary phases such as akermanite ($Ca_2MgSi_2O_7$), merwinite (Ca_3MgSiO_4), wollastonite ($CaSiO_3$), and silicon dioxide (SiO_2) was observed. This correlates with the appearance of exothermic peaks in the DSC

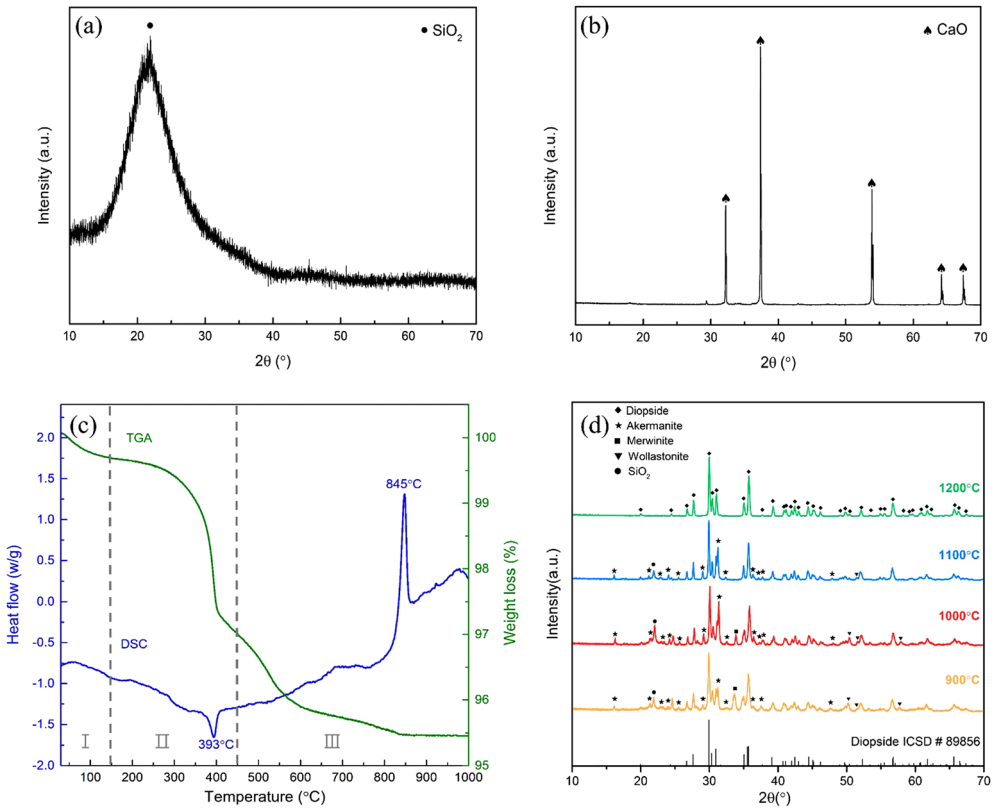

Fig. 2 (a) XRD pattern of rice husk after calcination at 700 °C for 6 h, (b) XRD pattern of eggshell after calcination at 900 °C for 2 h, (c) TGA/DSC curves of diopside precursor, and (d) XRD patterns of diopside sintered at different temperatures for 3 h.

analysis at the crystallization temperature of diopside (845 °C). As the sintering temperature increased to 1000 °C, diopside remained the dominant phase, but an exothermic peak was observed near 1000 °C in the DSC analysis, attributed to the intensification of secondary phases. At 1100 °C, diopside was still the main phase, but the peak intensity of the secondary phases began to decrease, with the merwinite peak disappearing. At 1200 °C, all secondary phases were completely eliminated, and the resulting composition was confirmed as pure diopside using Match3! software, corresponding to the standard reference (ICSD code: 89856). However, when the precursor was further sintered at 1300 °C, the sample melted and adhered to the crucible surface, despite the melting point of diopside being 1391 °C. This discrepancy may be due to temperature variations within the furnace chamber. Therefore, the optimal sintering temperature was determined to be 1200 °C.

3.2 Characterization of $MnFe_2O_4$ nanoparticles

The XRD pattern of the magnetic nanoparticles is shown in Fig. 3(a). No secondary phases were detected, and the cubic spinel structure, consistent with the standard ICSD code: 40702, confirms the formation of $MnFe_2O_4$. Additionally, the average crystalline size of the sample was estimated to be approximately 41 nm using Scherrer's formula[89] (eqn (7)).

$$D = \frac{K \times \gamma}{\beta \cos\theta} \quad (7)$$

where K is the shape factor, assumed to be 0.943 due to the cubic structure, γ is the X-ray wavelength, β is the full width at half maximum (FWHM) in radians, and θ is the Bragg angle.

The TEM image of $MnFe_2O_4$ nanoparticles is shown in Fig. 3(b), revealing the cuboctahedron-like morphology of the particles. Additionally, agglomeration can be observed, likely due to the absence of a surfactant during synthesis, leading to the formation of clusters as a result of magnetic coupling interactions between the nanoparticles. Based on the TEM images, the size distribution of 59 individual particles, measured using Nano Measurer, is presented in Fig. 3(c). The particle sizes mainly ranged from 30 to 65 nm, with a calculated average diameter of approximately 46 nm ± 22%, which closely aligns with the size estimated from XRD analysis.

3.3 Characterization of diopside–$MnFe_2O_4$ nanocomposites

Backscattered electron images (BEI) and quantitative chemical composition analysis of the sintered Di–*X*MnFe (*X* = 0, 10, 20, 30) nanocomposites are displayed in Fig. 4, with their physical properties summarized in Table 1. Fig. 4(a) and (e) show that the surface morphology of pure diopside consisted of agglomerated spherical particles ranging from 0.45 μm to 0.75 μm in size. In Fig. 4(i), the quantitative chemical composition analysis at site 1 confirmed the presence of oxides containing the essential elements Ca, Mg, and Si, with a molar ratio of 1 : 0.96 : 1.98. This ratio closely matches that of diopside ($CaMgSi_2O_6$), verifying that pure diopside can be synthesized from rice

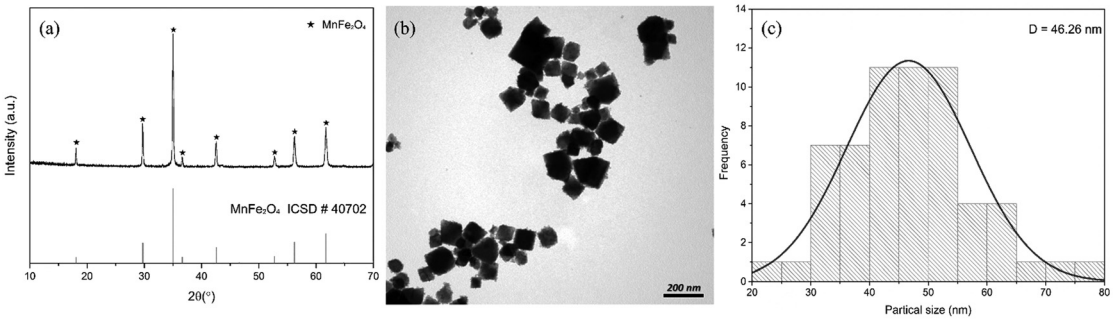

Fig. 3 (a) XRD pattern, (b) TEM image, and (c) particle size distribution of $MnFe_2O_4$ magnetic nanoparticles.

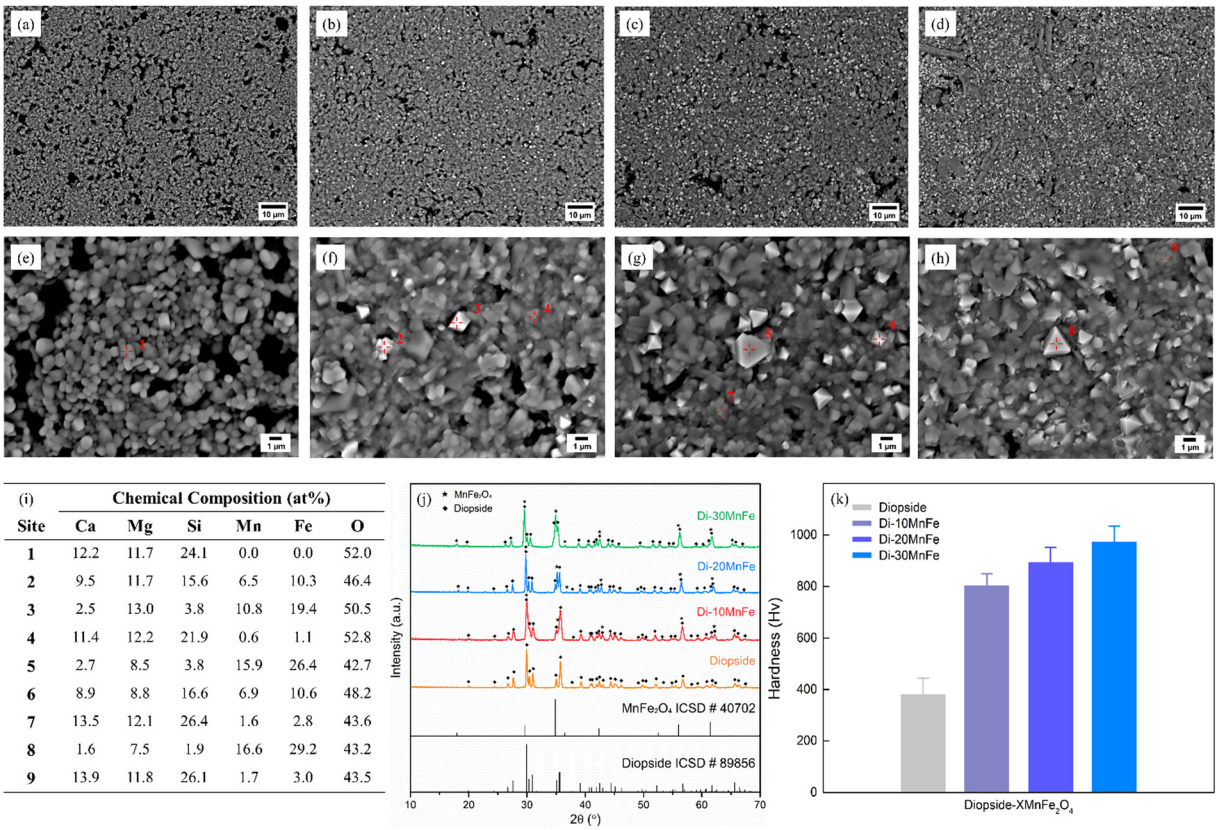

Fig. 4 Backscattered electron images of Di–*X*MnFe nanocomposites: (a), (e) *X* = 0 wt%, (b), (f) X = 10 wt%, (c), (g) *X* = 20 wt%, and (d), (h) *X* = 30 wt%. (i) Chemical compositions, (j) XRD patterns, and (k) hardness of Di–*X*MnFe nanocomposites (*X* = 0, 10, 20, and 30 wt%).

husk and eggshells sintered at 1200 °C. Additionally, pores were observed on the surface of the pure diopside, likely formed due to the release of volatile substances during the sintering process. These pores may enhance bioactivity and facilitate the release of ionic products.[90] The presence of microporosity (pores smaller than 10 μm) increases the surface area, which is believed to improve the adsorption of bone-inducing proteins and promote the formation of bone-like apatite through dissolution and reprecipitation processes.[91] Consequently, this porous surface morphology plays a crucial role in the interaction between bioceramic implants and surrounding tissues. In terms of density and porosity, Table 1 indicates that the apparent density (D_A) of diopside is 3.21 g cm^{-3}, which is quite close to its theoretical density of 3.26 g cm^{-3}. However, the bulk density (D_B) is significantly lower, at 2.55 g cm^{-3}. This discrepancy is attributed to the material's porosity, which was calculated to be 20.4%.

Fig. 4(b)–(d) and (f)–(h) display the backscattered electron images (BEI) of Di–*X*MnFe nanocomposites (*X* = 0, 10, 20, and 30). Due to the higher atomic numbers of Mn and Fe compared to Ca, Mg, and Si elements, $MnFe_2O_4$ appeared brighter in the BEI, allowing for clear differentiation between $MnFe_2O_4$ and $CaMgSi_2O_6$. As the concentration of $MnFe_2O_4$ magnetic nanoparticles increased, a greater number of angular particles,

Table 1 Density, porosity, and hardness of diopside–$MnFe_2O_4$ nanocomposites

	Composition (wt%)		Density (g cm^{-3})			
Sample	Diopside	$MnFe_2O_4$	Bulk (D_B)	Apparent (D_A)	Porosity (%)	Hardness (Hv)
Diopside	100	0	2.55	3.21	20.4	397.8 ± 47
Di–10MnFe	90	10	3.18	3.23	1.5	821.6 ± 27
Di–20MnFe	80	20	3.41	3.41	0.2	911.2 ± 40
Di–30MnFe	70	30	3.77	3.81	1.1	990.8 ± 44

uniformly distributed across the diopside surface, became visible. These $MnFe_2O_4$ nanoparticles exhibited a polyhedral morphology, which is consistent with the TEM image shown in Fig. 3(b). However, many of these grains grew from an average size of 46 nm to a range of 0.7–3.2 μm, forming a strong bond with the diopside matrix. The chemical composition analysis in Fig. 4(i) reveals that the brighter areas (sites 2, 3, 5, 6, and 8) corresponded to $MnFe_2O_4$. The elemental signals from the particles at sites 2 and 6 were more susceptible to interference from the surrounding diopside matrix due to their smaller size, resulting in compositions that included $CaMgSi_2O_6$. In contrast, the larger particles at sites 3, 5, and 8 displayed compositions more characteristic of pure $MnFe_2O_4$. However, Ca, Mg, and Si signals were also detected on these $MnFe_2O_4$ particles, with total concentrations ranging from 11 at% to 19.3 at%, indicating that co-sintering with $CaMgSi_2O_6$ led to the diffusion of Ca, Mg, and Si elements into $MnFe_2O_4$. Interestingly, a significant Mg content was found on the $MnFe_2O_4$ particles, likely due to the higher diffusivity of Mg^{2+} ions in oxides compared to Ca^{2+} and Si^{4+} ions, attributed to their smaller ionic radius and lower activation energy.[92] As the incorporation of $MnFe_2O_4$ nanoparticles increased, the sample surface became noticeably denser. Table 1 indicates that adding 10 wt% $MnFe_2O_4$ to diopside significantly reduced the porosity from 20.4% to 1.5%. Further increases in $MnFe_2O_4$ content to 20 and 30 wt% kept the porosity consistently around 1%. Moreover, in Fig. 4(i), sites 4, 7, and 9 represented the diopside matrix in the diopside–$MnFe_2O_4$ nanocomposites, with a confirmed chemical composition of Ca : Mg : Si at approximately 1 : 1 : 2. Notably, $MnFe_2O_4$ element signals were also detected in these sites, suggesting that nanoscale $MnFe_2O_4$ particles may be embedded between diopside grains. After sintering at 1200 °C, the high-temperature treatment facilitated element diffusion, causing the $MnFe_2O_4$ nanoparticles to bond tightly with the spherical diopside matrix and resulting in a denser structure with lower porosity. Consequently, the incorporation of $MnFe_2O_4$ nanoparticles significantly enhanced the sinterability of the diopside.

The XRD patterns of the sintered diopside–$MnFe_2O_4$ nanocomposites are presented in Fig. 4(j). All diffraction peaks could be indexed to the diopside phase ($CaMgSi_2O_6$, ICSD #89856) and the $MnFe_2O_4$ spinel phase (ICSD #40702), with no secondary phases such as Fe_2O_3, MnO, or amorphous impurities detected, indicating high phase purity. As the $MnFe_2O_4$ content increased, its characteristic peaks at 2θ values of 29.7°, 35.0°, 42.5°, 56.2°, and 61.7° became more prominent, while several of them overlapped with the main peaks of diopside. To further quantify the phase composition, Rietveld refinement was performed using Match! and FullProf Suite. The results revealed that the $MnFe_2O_4$ phase content increased proportionally with the nominal addition: 8.9% in Di–10MnFe, 17.1% in Di–20MnFe, and 26.3% in Di–30MnFe, with corresponding $CaMgSi_2O_6$ contents of 91.1%, 82.9%, and 73.7%, respectively. These values confirm that the majority of the ceramic matrix remains diopside, and the distribution of $MnFe_2O_4$ is consistent with the target formulation. However, the measured $MnFe_2O_4$ contents were slightly lower than the nominal values. This discrepancy may be attributed to partial material loss during ball milling, as $MnFe_2O_4$ possesses relatively high hardness and may become embedded into the milling jar walls or grinding media, thereby reducing the effective loading in the final mixture. In addition, a slight shift of $MnFe_2O_4$ diffraction peaks toward higher angles and diopside peaks toward lower angles was observed with increasing $MnFe_2O_4$ content. This trend is likely associated with mutual ionic diffusion during high-temperature sintering, as supported by the elemental analysis in Fig. 4(i). Smaller ions such as Mg^{2+}(0.57 Å) and Si^{4+}(0.26 Å)[93] may enter the $MnFe_2O_4$ lattice and induce lattice compression, while larger Mn^{2+}(0.66 Å) and Fe^{3+}(0.49 Å)[93] ions could diffuse into the $CaMgSi_2O_6$ lattice, causing lattice expansion. This interfacial diffusion contributes to the observed lattice distortion and partial peak shift behavior.

The hardness results of the Di–*X*MnFe nanocomposites (*X* = 0, 10, 20, and 30 wt%) after sintering are presented in Fig. 4(k) and Table 1. Each sample was measured at five different points on the pellet surface, and the values were used to calculate the mean and standard deviation. The hardness of the diopside–$MnFe_2O_4$ nanocomposites increased with the addition of magnetic nanoparticles. Remarkably, incorporating just 10 wt% of $MnFe_2O_4$ nearly doubled the hardness of diopside, significantly enhancing its mechanical properties. Increasing the $MnFe_2O_4$ content to 30 wt% further improved the hardness, reaching a maximum value up to 990.8 Hv. As shown in Table 1, the incorporation of magnetic nanoparticles reduced the porosity of the diopside, as observed in the SEM images. This densified crystalline structure is likely responsible for the material's excellent hardness. The influence of $MnFe_2O_4$ on the mechanical properties of Ca–Mg–Si-based bioceramics has not been reported in the literature. Comparable studies have focused on hydroxyapatite composites with added magnetite (Fe_3O_4),[94,95] where results showed that higher magnetite content increased porosity and reduced mechanical strength, which is contrary to our findings. When compared to densified (>93%) TCP bioceramics synthesized *via* novel ultrafast high-temperature sintering,[96] the hardness of our diopside–$MnFe_2O_4$ nanocomposites, enhanced by the densification effect of $MnFe_2O_4$, was considerably higher, with the densified TCP reaching a maximum hardness of only 350 Hv.

3.4 Magnetic property and magnetic hyperthermia ability of diopside–$MnFe_2O_4$ nanocomposites

The magnetic hysteresis (*M*–*H*) curves of $MnFe_2O_4$ nanoparticles and Di–*X*MnFe nanocomposites (*X* = 0, 10, 20, and

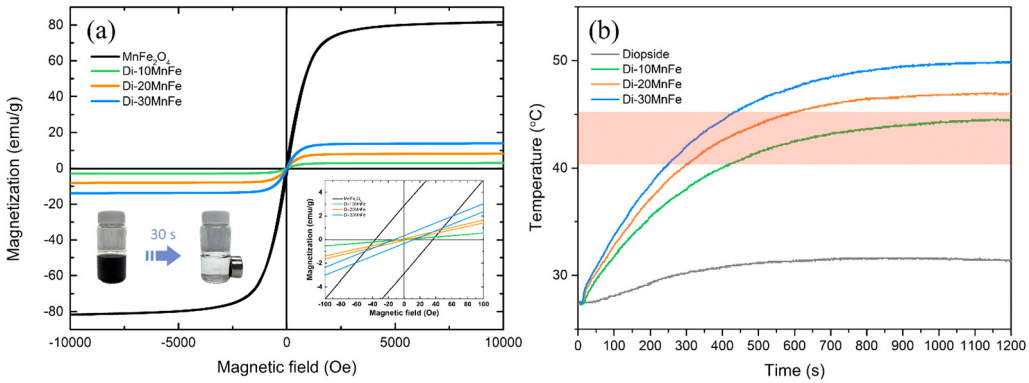

(c)

Sample	$MnFe_2O_4$	Di-10MnFe	Di-20MnFe	Di-30MnFe
Ms (emu/g)	81.60	2.99	8.14	13.94
SLP (W/g)	-	16.49	24.29	31.08

Fig. 5 (a) Magnetic hysteresis curves of $MnFe_2O_4$ and Di–*X*MnFe nanocomposites at 300 K (inset in the lower-right corner presenting a magnified view of the region within the ±100 Oe magnetic field range), (b) heating curves of Di–*X*MnFe nanocomposites for *in vitro* hyperthermia therapy (under a magnetic field of 30 Oe and an alternating current frequency of 287 kHz; the red shading indicates the hyperthermia therapy range), and (c) saturation magnetization (M_s), and specific loss power (SLP) values of Di–*X*MnFe nanocomposites (*X* = 0, 10, 20, and 30 wt%).

30 wt%) were measured under an external magnetic field ranging from ±10 000 Oe, as presented in Fig. 5. Additionally, the heating curves of Di–*X*MnFe nanocomposites for potential *in vitro* hyperthermia therapy are also shown. As illustrated in Fig. 5(a) and its inset, $MnFe_2O_4$ nanoparticles exhibited a coercivity (H_c) of approximately 36 Oe and a low remanence (M_r) of 3 emu g^{-1}, indicating that these nanoparticles possessed the characteristics of soft magnetic materials approaching a superparamagnetic state. This behavior suggests that the magnetization nearly returns to zero once the external magnetic field is removed, effectively minimizing magnetic dipolar interactions between particles. This is particularly advantageous in biomedical applications, as it prevents particle aggregation, which could otherwise lead to adverse effects such as blood clots in the circulatory system. Notably, the saturation magnetization (M_s) of the $MnFe_2O_4$ nanoparticles synthesized in this study reached 81.6 emu g^{-1} at room temperature, achieving 99.5% of the bulk $MnFe_2O_4$ value (M_s = 82.0 emu g^{-1}). This value is significantly higher than those reported for $MnFe_2O_4$ nanoparticles in previous studies (16.2–76 emu g^{-1} (ref. 51,55,63,77,81 and 97–102), making this material the highest-performing $MnFe_2O_4$ nanoparticle currently published. This extraordinary M_s value indicates the superior magnetic performance of the synthesized nanoparticles and their potential for efficient heating in hyperthermia applications.

It is well known that as the particle size of magnetic materials decreases to the nanoscale, the increased surface-to-volume ratio enhances surface effects (*e.g.*, surface spin disorder and magnetic dead layers).[103] Concurrently, thermal fluctuations increasingly affect the magnetic moments, disrupting their alignment and often leading to a decline in saturation magnetization (M_s).[103] However, the $MnFe_2O_4$ nanoparticles synthesized in this study demonstrated an M_s value comparable to that of bulk $MnFe_2O_4$, indicating that particle size reduction did not significantly impair the magnetic properties. This exceptional performance can be attributed to several key factors, as follows. (1) As confirmed by the XRD patterns (Fig. 3(a)), the $MnFe_2O_4$ nanoparticles exhibited sharp and well-defined diffraction peaks, closely matching the standard $MnFe_2O_4$ pattern (ICSD #40702) without any additional peaks, which would indicate secondary phases (*e.g.*, Fe_2O_3 or MnO). This confirms the high purity and structural integrity of the synthesized nanoparticles, ensuring that the internal magnetic moment alignment remained highly ordered, similar to bulk materials. (2) TEM images and particle size distribution (Fig. 3(b) and (c)) reveal that the $MnFe_2O_4$ nanoparticles exhibited clear particle boundaries, good dispersion, and minimal aggregation. The low degree of surface defects (*e.g.*, lattice distortions or chemical adsorptions) reduced their surface spin disorder, contributing to the high M_s. Additionally, the narrow size distribution (40–55 nm, average size: 46 nm) reflected stable synthesis conditions and uniform particles, further ensuring that the overall magnetic behavior closely resembled that of bulk $MnFe_2O_4$. The cuboctahedron-like morphology of the nanoparticles may also contribute to their high M_s. This is supported by findings from Noh *et al.*,[104] which reported that cubic magnetic nanoparticles exhibited lower surface anisotropy compared to spherical ones, thereby enabling higher saturation magnetization for cubic-shaped nanoparticles. (3) The average particle size of 46 nm approached the single-domain critical size of $MnFe_2O_4$, where particles typically exhibit uniform magnetic alignment.[67] However, the particle size of 46 nm remained larger than the superparamagnetic critical size, as evidenced by the non-zero H_c and M_r in the *M*–*H* curves. Unlike bulk $MnFe_2O_4$, which has a multi-domain

structure and lower H_c due to the ease of domain wall motion, single-domain nanoparticles lack domain walls. The magnetic moments in these nanoparticles flip coherently as a whole, rather than through domain wall movement. This coherent flipping mechanism requires overcoming higher energy barriers, leading to slightly higher coercivity compared to bulk materials.[103] Consequently, the single-domain structure of $MnFe_2O_4$ nanoparticles synthesized in this study eliminated the influence of domain walls (*e.g.*, pinning effects), thereby contributing to their enhanced saturation magnetization. (4) The average size of 46 nm provided a relatively low surface-to-volume ratio, minimizing the influence of surface spin disorder. While some degree of surface spin misalignment may exist, the contribution of the well-ordered internal magnetic moments effectively compensated for surface-induced magnetic loss. This optimal size prevented significant magnetic degradation caused by surface effects, while also avoiding the energy dissipation associated with multi-domain structures in bulk materials.

When $MnFe_2O_4$ nanoparticles were incorporated into $CaMgSi_2O_6$ to form composites, the M_s, H_c, and M_r values decreased significantly as the $MnFe_2O_4$ content decreased. This trend can be explained by the following mechanisms. (1) The inclusion of non-magnetic $CaMgSi_2O_6$ diluted the concentration of magnetic $MnFe_2O_4$ particles, leading to a proportional reduction in the overall M_s. (2) The dispersion of $MnFe_2O_4$ nanoparticles within the ceramic matrix reduced interparticle magnetic dipole interactions, which impaired cooperative magnetic moment alignment under an external field, particularly in the low-field region. (3) The reduced interparticle magnetic coupling due to matrix separation weakened the collective magnetic anisotropy barriers, making moment reversal easier and resulting in a lower H_c. (4) After the removal of the external magnetic field, the magnetic isolation imposed by the non-magnetic matrix diminished remanent coupling among $MnFe_2O_4$ particles, thereby reducing the stability of magnetic alignment and leading to a decrease in M_r. (5) During high-temperature sintering, the growth of $MnFe_2O_4$ grains introduced grain boundaries, while the diffusion of Ca, Mg, and Si into the $MnFe_2O_4$ phase induced lattice distortions, as evidenced by Fig. 4(i) and (j). In addition, grain coarsening induced by sintering may have promoted partial transition from single-domain to multi-domain states, which would lower the coercivity (H_c) due to the increased ease of domain wall motion compared to coherent rotation in single-domain particles. These factors likely disrupted the alignment of magnetic moments, increased local spin disorder, and further reduced M_s, H_c, and M_r. In summary, both compositional dilution and microstructural evolution, including particle size growth and matrix-induced isolation, contribute to the observed variation in magnetic behavior among the Di–*X*MnFe composites.

The $MnFe_2O_4$ nanoparticles synthesized in this study demonstrated a near-bulk saturation magnetization (M_s) at the nanoscale, due to their excellent crystallinity, high purity, particle shape, single-domain behavior, and minimized surface effects. Upon integration with $CaMgSi_2O_6$, the magnetic properties of the composites decreased predictably due to magnetic dilution, weakened interparticle interactions, and structural alterations.

Fig. 5(b) illustrates the heating rates of Di–*X*MnFe nanocomposites (X = 0, 10, 20, and 30 wt%) under a magnetic field of 30 Oe and an alternating current frequency of 287 kHz, while their specific loss power (SLP) values are presented in Fig. 5(c). To ensure the safety of healthy human tissues, Hergt *et al.*,[105] building on Brezovich *et al.*'s research,[106] proposed that the product of the magnetic field amplitude (H) and frequency (f) should not exceed 5×10^9 A m^{-1} s^{-1}. Within this limit, individuals can tolerate magnetic hyperthermia for over an hour without discomfort. Furthermore, the operational frequency for magnetic hyperthermia is typically restricted to a narrow range of 100–300 kHz.[59] The magnetic field amplitude and frequency used in this study were 30 Oe (= 2.4 kA m^{-1}) and 287 kHz, resulting in $H \times f = 6.9 \times 10^8$ A m^{-1} s^{-1}, which is well within the safe range. As shown in Fig. 5(b), the temperature of the aqueous solution containing diopside increased to 30 °C within 5 minutes under the alternating magnetic field. This slight temperature rise can be attributed to ambient heating caused by the operation of the equipment, as diopside itself does not induce heating under magnetic fields. For the Di–MnFe nanocomposites, the heating rate was positively correlated with the $MnFe_2O_4$ content, and all samples achieved the therapeutic hyperthermia range of 41–46 °C. Notably, the heating curve of Di–10MnFe reached 41 °C in 7.7 minutes and maintained the temperature within this therapeutic window for up to 20 minutes without exceeding 46 °C, making it an optimal formulation for hyperthermia applications. This is particularly advantageous because achieving effective hyperthermia with a lower content of magnetic nanoparticles reduces potential toxicity and cost, thereby making high-efficiency heating nanoparticles more desirable.[99] In addition, the steady-state temperature of Di–10MnFe was approximately 44.5 °C, which falls within the recommended temperature range (41–45 °C) for mild photothermal therapy (MPT) to support bone tissue regeneration.[61] Within this temperature window, osteogenesis has been reported to be enhanced. Moreover, to evaluate the heating efficiency of Di–MnFe nanocomposites, the SLP of the samples under the alternating magnetic field was calculated using the initial slope method. The results were 16.49, 24.29, and 31.08 W g^{-1} for Di–10MnFe, Di–20MnFe, and Di–30MnFe, respectively, as shown in Fig. 5(c).

The heat generation mechanisms of Di–MnFe nanocomposites are elucidated as follows. The increase in $MnFe_2O_4$ content elevated the proportion of magnetic phases, total magnetic moments, and saturation magnetization (M_s), leading to a significant rise in SLP. The high M_s suggests the superior heating efficiency of $MnFe_2O_4$ nanoparticles. However, the increase in SLP was disproportionate to the rise in M_s, indicating the involvement of additional factors. Heat generation mechanisms in magnetic materials under an alternating magnetic field primarily include: (1) magnetic hysteresis loss, (2) Néel relaxation loss, and (3) Brownian relaxation loss. Among these mechanisms, Brownian relaxation loss, where heat is generated through the physical rotation of magnetic

nanoparticles due to friction with the surrounding medium, can be excluded in this study. This is because the $MnFe_2O_4$ nanoparticles were tightly bonded with $CaMgSi_2O_6$ during high-temperature sintering, making physical rotation unlikely and thus eliminating Brownian relaxation loss as a contributor to heat generation. Fig. 5(a) shows that as the $MnFe_2O_4$ content increased, the area enclosed by the hysteresis loop also grew, indicating more heat generation from hysteresis loss. From the above mechanism analysis, it can be inferred that while increasing the $MnFe_2O_4$ content enhanced the overall magnetic moment and generated heat through magnetic hysteresis loss, the SLP did not increase proportionally. This suggests that the heat contribution from Néel relaxation loss may decrease as the $MnFe_2O_4$ content increased. Néel relaxation involves the internal rotation of magnetic moments within particles under an alternating magnetic field, producing heat through friction with the crystal lattice. As shown in the inset of Fig. 5(a), the coercivity (H_c) increased with higher $MnFe_2O_4$ content. This is likely attributed to particle aggregation, leading to magnetic moment coupling and raising the energy barriers required for flipping the magnetic moments. Additionally, grain growth and the diffusion of non-magnetic elements (*e.g.*, Ca, Mg, Si) into the magnetic particles during high-temperature sintering introduced grain boundaries and lattice stress or distortions, further increasing magnetic anisotropy and coercivity. These factors diminished Néel relaxation efficiency by lowering the frequency of magnetic moment flipping and stabilizing the magnetic moments against thermal disturbances.

The $MnFe_2O_4$ nanoparticles synthesized in this study demonstrated excellent magnetic performance. When incorporated into $CaMgSi_2O_6$ to form composites, even at a low concentration of 10 wt%, the resulting Di–10MnFe nanocomposites retained a functional saturation magnetization (M_s) and negligible coercivity (H_c). This combination allowed the Di–10MnFe nanocomposites to achieve sufficient heating within the hyperthermia temperature range solely through Néel relaxation loss, using fewer magnetic nanoparticles. Although higher additions of $MnFe_2O_4$ increased the total SLP, the enhancement in heating efficiency became marginal with excessive loading. These findings suggest that $MnFe_2O_4$ nanoparticles can serve as efficient heat sources in various biological environments by optimizing the magnetic field parameters and nanoparticle concentration.[62]

3.5 Cell viability and proliferation of diopside–$MnFe_2O_4$ nanocomposites

The effects of ionic extracts from Di–*X*MnFe nanocomposites (X = 0, 10, 20, 30 wt%) on MC3T3-E1 cell viability and proliferation were evaluated over 1, 3, and 7 days of culture using the MTT assay, with the results shown in Fig. 6. According to the biological evaluation of medical devices (ISO 10993-5: 2009[107]), a material is considered cytotoxic if the relative cell viability after incubation is less than 70%. As shown in Fig. 6(a), the MTT cytotoxicity test results for MC3T3-E1 cultured with diopside–$MnFe_2O_4$ nanocomposites indicate that diopside synthesized from rice husks and eggshells exhibited no cytotoxicity and demonstrated excellent cell compatibility. These findings align with previous reports that diopside derived from biowaste showed good biocompatibility.[11] Furthermore, the addition of $MnFe_2O_4$ magnetic nanoparticles to the bioceramic composites did not introduce cytotoxicity and even enhanced cell compatibility. Among these, Di–30MnFe exhibited a significant difference compared to the blank control group ($P < 0.05$), consistent with earlier studies reporting that Fe_3O_4 magnetic nanoparticles incorporated into bioceramics also maintained good cell compatibility.[47,56]

Fig. 6(b) presents the results of MC3T3-E1 cell proliferation over 1, 3, and 7 days cultured with diopside–$MnFe_2O_4$ nanocomposites. The diopside synthesized from biowaste in this study demonstrated excellent cell proliferation effects, consistent with prior research showing comparable proliferation rates with different cell types, such as Saos-2, HUVECs, and fibroblasts,[108] and similar proliferation levels to those observed with TCP and HAp.[24] Bioceramics with added $MnFe_2O_4$

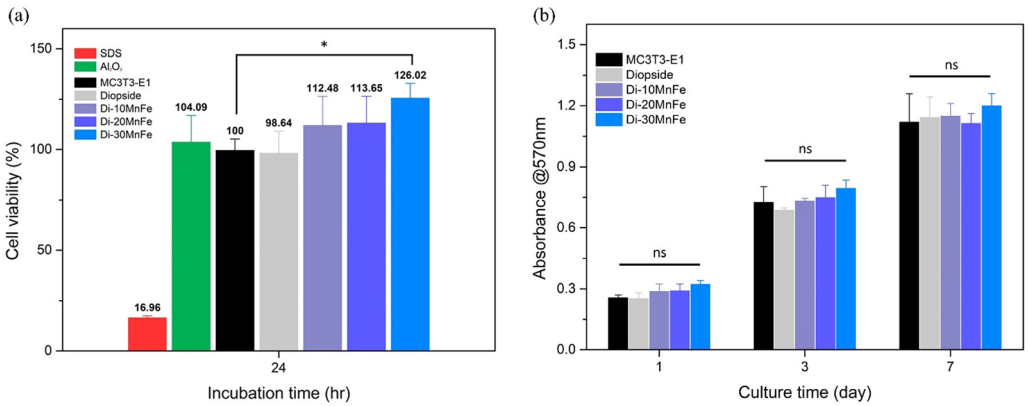

Fig. 6 (a) MTT results of Di–*X*MnFe nanocomposites (X = 0, 10, 20, 30 wt%) on MC3T3-E1 cells for 24 h (ANOVA, MC3T3-E1 cell control group compared to four nanocomposites, *$P < 0.05$; **$P < 0.01$; ***$P < 0.001$; n = 6), (b) proliferation of Di–*X*MnFe nanocomposites (X = 0, 10, 20, 30 wt%) on MC3T3-E1 cells measured at 1, 3 and 7 days (ANOVA, MC3T3-E1 cell control group compared to four nanocomposites, *$P < 0.05$; **$P < 0.01$; ***$P < 0.001$; n = 4).

nanoparticles also supported cell proliferation over time. In this study, all three groups exhibited good MC3T3-E1 proliferation, with minor variations between groups, yet maintaining high proliferation levels overall. There were no significant differences among the diopside–$MnFe_2O_4$ nanocomposite groups on days 1, 3, and 7 ($P > 0.05$), indicating that the addition of $MnFe_2O_4$ magnetic nanoparticles did not negatively affect cell proliferation. These results are in line with previous findings, where bioceramics containing Fe_3O_4 magnetic nanoparticles supported sustained high levels of cell proliferation.[47,56] This could be attributed to the release of Fe^{2+}/Fe^{3+} ions from $MnFe_2O_4$ nanoparticles, which may regulate intracellular oxidative stress by mimicking peroxidase activity and reducing hydrogen peroxide levels, thereby promoting cell cycle progression in osteoprogenitor cells.[74]

3.6 Alkaline phosphatase assay (ALP) of diopside–$MnFe_2O_4$ nanocomposites

In vitro differentiation of osteoblasts and subsequent bone formation is a progressive process characterized by three main stages: cell proliferation, extracellular matrix production and maturation, and mineralization.[109] Alkaline phosphatase (ALP) is a key marker of early osteoblast differentiation. In this study, the ALP activity of MC3T3-E1 cells cultured with the extract of Di–*X*MnFe nanocomposites (X = 0, 10, 20, 30 wt%) for 7 and 14 days was evaluated. The ALP activity was quantified using ImageJ software for precise analysis.[110]

The staining results of ALP activity are shown in Fig. 7(a), and the corresponding quantitative analysis is presented in Fig. 7(b). As indicated in Fig. 7(b), the ALP activity of the osteogenic induction medium (OIM) control group and the four diopside–$MnFe_2O_4$ nanocomposite groups showed no significant difference after 7 days of culture ($P > 0.05$). This observation is consistent with the cell proliferation results on day 7 shown in Fig. 6(b). However, by day 14, the Di–30MnFe nanocomposite exhibited a significant increase in ALP activity compared to other groups ($P < 0.001$). According to previous studies, ALP activity peaked as osteoblasts matured and then declined as mineralization began.[111] For instance, Yeniyol *et al.*[112] reported that the ALP activity of MC3T3-E1 cells typically peaked between days 9 and 12 before decreasing after day 12, corresponding to the onset of extracellular matrix deposition and mineralization. Based on the results of this study, it can be inferred that the addition of $MnFe_2O_4$ magnetic nanoparticles accelerated the maturation of MC3T3-E1 cells. The observed decrease in ALP activity at later stages suggests the initiation of matrix mineralization. Furthermore, Zhang *et al.*[56] noted that Fe_3O_4 could stimulate ALP activity in human bone marrow stromal cells (h-BMSCs). Similarly, Wu *et al.*[113] demonstrated that magnetic nanoparticles incorporated into Ca–P ceramics enhanced osteoblasts (Ros17/2.8 and MG-63) proliferation and differentiation while upregulating rhBMP-2 expression, ultimately promoting bone tissue formation. Moreover, Yu *et al.*[73] reported that Mn-containing stainless steel significantly increased ALP expression and activity in rBMSCs by activating the ERK1/2 signaling pathway, thereby promoting early-stage osteogenic differentiation. These findings align with the results of the present study, underscoring the potential of $MnFe_2O_4$ magnetic nanoparticles to enhance early osteogenic activity and bone formation.

3.7 Alizarin Red S mineralization assay (ARS) of diopside–$MnFe_2O_4$ nanocomposites

The present study evaluated bone mineralization in MC3T3-E1 cells cultured with the extract of Di–*X*MnFe nanocomposites

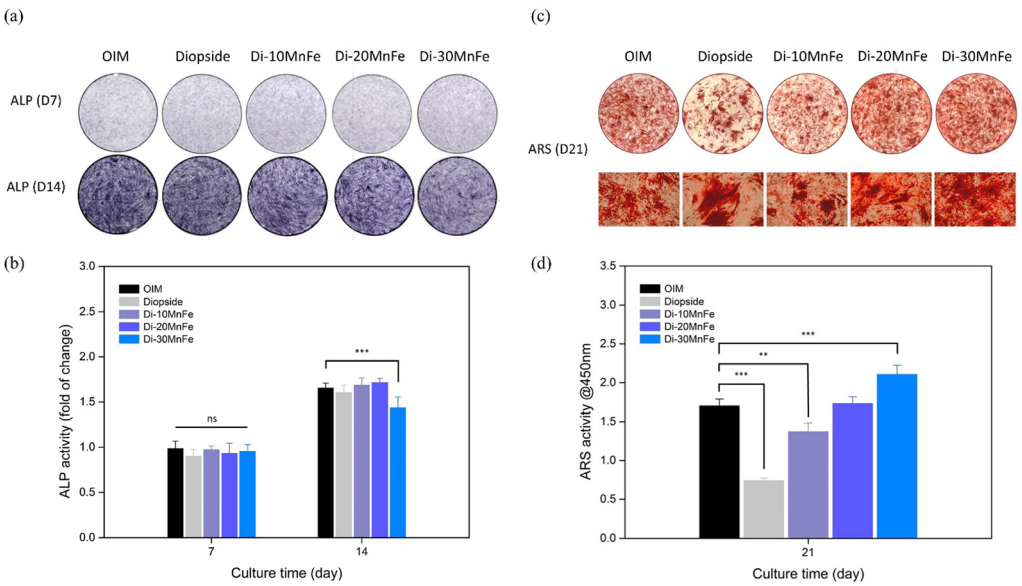

Fig. 7 (a) ALP activity of Di–*X*MnFe nanocomposites (X = 0, 10, 20, 30 wt%) on MC3T3-E1 cells measured at 7 and 14 days, and (b) quantitative analysis (ANOVA, OIM control group compared to four nanocomposites, *$P < 0.05$; **$P < 0.01$; ***$P < 0.001$; n = 5). (c) ARS mineralization of Di–*X*MnFe nanocomposites (X = 0, 10, 20, 30 wt%) on MC3T3-E1 cells measured at 21 days, and (d) quantitative analysis (ANOVA, OIM control group compared to four nanocomposites, *$P < 0.05$; **$P < 0.01$; ***$P < 0.001$; n = 3).

(X = 0, 10, 20, 30 wt%) for 21 days using Alizarin Red S (ARS) staining. As shown in Fig. 7(c) and (d), the mineralization results aligned with the ALP activity findings, indicating that the incorporation of $MnFe_2O_4$ magnetic nanoparticles enhanced osteogenic differentiation in MC3T3-E1 cells, which subsequently influenced bone mineralization after 21 days of culture. Although the mineralization performance of the diopside bioceramic alone was lower than that of the osteogenic induction medium (OIM) control group, the three groups of diopside–$MnFe_2O_4$ nanocomposites exhibited a positive correlation between $MnFe_2O_4$ content and mineralization. Notably, the Di–30MnFe nanocomposite exhibited superior mineralization performance among all samples and demonstrated significant differences compared to the control group ($P < 0.001$). This observation is supported by a study conducted by Li *et al.*,[114] which reported that Mn^{2+} ions released from Mn-doped β-tricalcium phosphate (TCP) bioceramics can significantly inhibit osteoclast formation and activity while promoting osteoblast differentiation and accelerating bone regeneration. Similarly, Yu *et al.*[73] demonstrated that the release of Mn^{2+} from Mn-containing stainless steel enhanced matrix mineralization in rBMSCs, which was accompanied by the upregulation of both early (ALP) and later-stage (OCN) osteogenic markers through activation of the ERK1/2 signaling pathway. Based on these findings, diopside–$MnFe_2O_4$ nanocomposites developed in this study may represent a more promising alternative compared to Fe_3O_4 magnetic nanoparticle-based bioceramics.

Although the incorporation of 20–30 wt% $MnFe_2O_4$ content enhanced mechanical strength and osteogenic activity in this study, a trade-off may occur at concentrations beyond this range. Excessive $MnFe_2O_4$ loading may improve mechanical integrity through phase reinforcement, but could also reduce the Ca content in the ceramic matrix, which is crucial for bone regeneration. This Ca deficiency may compromise biocompatibility or osteoinductivity. Conversely, lower $MnFe_2O_4$ content (<10 wt%) may result in insufficient heating performance, while higher content (≥20 wt%) leads to overly rapid temperature rise, as observed in Fig. 5(b). Notably, the Di–10MnFe sample maintained a steady temperature of ~44.5 °C over 20 minutes without exceeding 46 °C, which aligns with typical hyperthermia treatment durations.[115] In contrast, the 20 and 30 wt% groups exceeded 46 °C within 10 minutes, which may pose a risk of thermal damage to surrounding healthy tissues. While these results were obtained from *in vitro* testing, previous studies have shown that *in vivo* magnetothermal heating tends to be 1.0–3.5 °C lower due to heat dissipation by tissue conduction and local blood perfusion.[116] Therefore, the Di–10MnFe formulation is expected to generate temperatures within the therapeutic range of 41–46 °C *in vivo*, making it a promising candidate for safe clinical application. These findings suggest that ~10 wt% $MnFe_2O_4$ may represent a thermally safe and biologically favorable threshold for balancing heating efficiency, biocompatibility, and structural integrity.

3.8 Limitations & future perspectives

Although this study provides comprehensive *in vitro* evidence supporting the biocompatibility, osteogenic activity, and magnetothermal potential of diopside–$MnFe_2O_4$ nanocomposites, several limitations remain that warrant further investigation. All experiments related to biological performance were conducted under *in vitro* conditions using MC3T3-E1 pre-osteoblasts, which only partially replicate the physiological microenvironment. Therefore, the long-term behavior of the nanocomposites *in vivo*, including their degradation, biodistribution, and systemic biocompatibility, remains to be validated. In particular, the fate of released Mn^{2+} and Fe^{2+}/Fe^{3+} ions after implantation requires further study, as excessive accumulation of transition metals in major organs may pose toxicological risks. A recent review similarly emphasized that the long-term toxicity of $MnFe_2O_4$ nanomaterials in living systems remains largely unexplored and needs to be thoroughly assessed in future studies.[67] In addition, the therapeutic efficacy of the nanocomposites for magnetothermal tumor ablation has not yet been confirmed under *in vivo* magnetic field conditions.

Future work will therefore focus on animal experiments to evaluate the biosafety, ion metabolism, osteointegration, and bone regeneration capacity of the nanocomposites in critical-sized defect models. Simultaneously, *in vivo* hyperthermia studies under clinically relevant AC magnetic field exposure will be conducted to verify the dual functionality of the system for both tumor ablation and bone tissue repair. These considerations not only address current limitations but also guide future optimization of $MnFe_2O_4$-based multifunctional platforms for clinical translation.

To ensure safety and efficacy in practical use, real-time temperature monitoring strategies such as fiber optic thermometry, magnetic resonance thermometry (MRT), ultrasound-based thermometry, and infrared thermal imaging can be employed. Among them, fiber optic thermometry is particularly advantageous due to its high sensitivity, lack of electromagnetic interference, and compatibility with MRI-guided setups.[117] These approaches, when combined with feedback-controlled AMF systems, can help maintain thermal precision during hyperthermia treatments. In addition, the long-term stability of $MnFe_2O_4$ nanoparticles under physiological conditions is an important consideration. Although spinel ferrites such as $MnFe_2O_4$ are generally more chemically stable than Fe_3O_4, partial dissolution or oxidative degradation may occur over extended implantation or storage periods. To address this, surface modification strategies (*e.g.*, silica coating and polymer encapsulation) and composite embedding, as employed in this study, can help minimize direct exposure to fluids and preserve both magnetic performance and biocompatibility over time.[56]

In addition to *in vivo* evaluations and magnetic control, processing parameters such as sintering dwell-time may also play a crucial role in determining the microstructure and functional performance of the nanocomposites. Variations in dwell-time can influence grain growth, densification, interfacial bonding, and magnetic behavior. Although this study focused on a fixed sintering duration, future work may investigate the effects of different thermal profiles to further optimize the balance between mechanical strength, magnetic properties, and biocompatibility.

4. Conclusion

This study pioneers the integration of $MnFe_2O_4$ nanoparticles into diopside bioceramics, advancing the development of multifunctional nanocomposites with outstanding biomedical properties, such as bone defect repair with load-bearing support and hyperthermia therapy. By utilizing biowaste-derived precursors, eggshells as a calcium source and rice husks as a silica source, high-purity diopside was efficiently synthesized through a solid-state reaction with an optimal sintering temperature of 1200 °C. This sustainable approach not only mitigates environmental concerns but also delivers a mechanically robust bioceramic base suitable for composite fabrication.

Remarkably, $MnFe_2O_4$ nanoparticles with an average particle size of 46 nm were synthesized using a facile hydrothermal method combined with magnetic separation, achieving an impressive saturation magnetization (M_s) of 81.6 emu g^{-1}. This M_s, accounting for 99.5% of bulk $MnFe_2O_4$, stands as the highest value reported in the literature to date. Such exceptional magnetic performance can be attributed to the nanoparticles' excellent crystallinity, high purity, cuboctahedral morphology, single-domain behavior, and minimal surface effects.

The incorporation of $MnFe_2O_4$ nanoparticles into diopside (Di–MnFe nanocomposites) significantly enhanced diopside's physical and mechanical properties, including improved sinterability, increased density, and a remarkable 2–2.5-fold enhancement in hardness, while reducing porosity to approximately 1%. Notably, adding just 10 wt% $MnFe_2O_4$ was sufficient to achieve hyperthermia efficacy within the safe therapeutic temperature range (41–46 °C) under an alternating magnetic field of 30 Oe and 287 kHz, solely driven by Néel relaxation mechanisms, with near-zero coercivity.

Biocompatibility evaluations confirmed that $MnFe_2O_4$ inclusion caused no cytotoxicity, while further promoting osteoblast differentiation and mineralization, as evidenced by elevated ALP activity and ARS staining. Impressively, all Di–MnFe nanocomposites exhibited superior osteogenic performance, underscoring their potential applications in osteosarcoma treatment and bone regeneration. These findings position diopside–$MnFe_2O_4$ nanocomposites as promising candidates for advanced orthopedic and oncological therapies, seamlessly combining sustainable material synthesis with exceptional functional properties.

Author contributions

Guan-Xiang Liao: methodology, investigation, data curation, formal analysis, writing – original draft. Wei-Hsi Chang: resource, investigation, funding acquisition. Yu-Sheng Tseng: investigation, data curation, formal analysis, writing – review & editing. Wen-Fan Chen: conceptualization, methodology, investigation, funding acquisition, writing – original draft, supervision.

Conflicts of interest

The authors declare no conflict of interest.

Data availability

All data underlying the results are available as part of the article and no additional source data are required.

Acknowledgements

National Science and Technology Council of Taiwan under contract NSTC 112-2636-E-110-006, and Kaohsiung Armed Forces General Hospital grant number KAFGH_D_112013. The authors are thankful for the Field Emission Electron Probe Microanalyzer provided by the Joint Center for High Valued Instruments at National Sun Yat-Sen University in Taiwan, the Superconductor Quantum Interference Device at Instrument Center of National Cheng Kung University in Taiwan, Miss Ting-Yin Cheng at the Instrumentation Centre of National Tsing Hua University in Taiwan for the Thermogravimetric analysis (TGA), Transmission Electron Microscopy provided by the Instrumentation Center of National Taiwan University, and the National Center for High-performance Computing (NCHC) for providing computational and storage resources.

References

1 L. Rozeman, A. Cleton-Jansen and P. Hogendoorn, Pathology of primary malignant bone and cartilage tumours, *Int. Orthop.*, 2006, **30**, 437–444.
2 J. Ritter and S. Bielack, Osteosarcoma, *Ann. Oncol.*, 2010, **21**, vii320–vii325.
3 A. M. Czarnecka, K. Synoradzki, W. Firlej, E. Bartnik, P. Sobczuk, M. Fiedorowicz, P. Grieb and P. Rutkowski, Molecular biology of osteosarcoma, *Cancers*, 2020, **12**(8), 2130.
4 L. M. Kelley, M. Schlegel, S. Hecker-Nolting, M. Kevric, B. Haller, C. Rössig, P. Reichardt, L. Kager, T. Kühne, G. Gosheger, R. Windhager, K. Specht, H. Rechl, P.-U. Tunn, D. Baumhoer, T. Wirth, M. Werner, Tv Kalle, M. Nathrath, S. Burdach, S. Bielack and Iv Lüttichau, Pathological fracture and prognosis of high-grade osteosarcoma of the extremities: An analysis of 2847 consecutive cooperative osteosarcoma study group (COSS) patients, *J. Clin. Oncol.*, 2020, **38**(8), 823–833.
5 G. Ottaviani and N. Jaffe, The epidemiology of osteosarcoma, *Pediatric and adolescent osteosarcoma*, Springer, Boston, 2010, pp. 3–13.
6 J. Y. Wang, P. K. Wu, P. C. H. Chen, C. C. Yen, G. Y. Hung, C. F. Chen, S. C. Hung, S. F. Tsai, C. L. Liu, T. H. Chen and W.-M. Chen, Manipulation therapy prior to diagnosis induced primary osteosarcoma metastasis—from clinical to basic research, *PLoS One*, 2014, **9**(5), e96571.
7 A. Luetke, P. A. Meyers, I. Lewis and H. Juergens, Osteosarcoma treatment–where do we stand? A state of the art review, *Cancer Treat. Rev.*, 2014, **40**(4), 523–532.
8 U. Anand, A. Dey, A. K. S. Chandel, R. Sanyal, A. Mishra, D. K. Pandey, V. De Falco, A. Upadhyay, R. Kandimalla, A. Chaudhary, J. K. Dhanjal, S. Dewanjee, J. Vallamkondu

and J. M. Pérez de la Lastra, Cancer chemotherapy and beyond: Current status, drug candidates, associated risks and progress in targeted therapeutics, *Genes Dis.*, 2023, **10**(4), 1367–1401.

9 T. Winkler, F. A. Sass, G. N. Duda and K. Schmidt-Bleek, A review of biomaterials in bone defect healing, remaining shortcomings and future opportunities for bone tissue engineering: The unsolved challenge, *Bone Joint Res.*, 2018, **7**(3), 232–243.

10 C. Gao, S. Peng, P. Feng and C. Shuai, Bone biomaterials and interactions with stem cells, *Bone Res.*, 2017, **5**(1), 17059.

11 P. Srinath, P. A. Azeem, K. V. Reddy, P. Chiranjeevi, M. Bramanandam and R. P. Rao, A novel cost-effective approach to fabricate diopside bioceramics: A promising ceramics for orthopedic applications, *Adv. Powder Technol.*, 2021, **32**(3), 875–884.

12 W. F. Ho, H. C. Hsu, S. K. Hsu, C. W. Hung and S. C. Wu, Calcium phosphate bioceramics synthesized from eggshell powders through a solid state reaction, *Ceram. Int.*, 2013, **39**(6), 6467–6473.

13 R. Choudhary, S. K. Venkatraman, I. Bulygina, F. Senatov, S. Kaloshkin, N. Anisimova, M. Kiselevskiy, M. Knyazeva, D. Kukui and F. Walther, Biomineralization, dissolution and cellular studies of silicate bioceramics prepared from eggshell and rice husk, *Mater. Sci. Eng., C*, 2021, **118**, 111456.

14 A. Kazemi, M. Abdellahi, A. Khajeh-Sharafabadi, A. Khandan and N. Ozada, Study of *in vitro* bioactivity and mechanical properties of diopside nano-bioceramic synthesized by a facile method using eggshell as raw material, *Mater. Sci. Eng., C*, 2017, **71**, 604–610.

15 D. V. Abere, S. A. Ojo, G. M. Oyatogun, M. B. Paredes-Epinosa, M. C. D. Niluxsshun and A. Hakami, Mechanical and morphological characterization of nano-hydroxyapatite (nHA) for bone regeneration: A mini review, *Biomed. Eng. Adv.*, 2022, **4**, 100056.

16 I. Ielo, G. Calabrese, G. De Luca and S. Conoci, Recent advances in hydroxyapatite-based biocomposites for bone tissue regeneration in orthopedics, *Int. J. Mol. Sci.*, 2022, **23**(17), 9721.

17 P. Srinath, P. Abdul Azeem and K. Venugopal Reddy, Review on calcium silicate-based bioceramics in bone tissue engineering, *Int. J. Appl. Ceram. Technol.*, 2020, **17**(5), 2450–2464.

18 K. Bavya Devi, S. K. Nandi and M. Roy, Magnesium silicate bioceramics for bone regeneration: A review, *J. Indian Inst. Sci.*, 2019, **99**, 261–288.

19 M. Ahmadipour, H. Mohammadi, A. L. Pang, M. Arjmand, T. Ayode Otitoju, P. U. Okoye and B. Rajitha, A review: Silicate ceramic-polymer composite scaffold for bone tissue engineering, *Int. J. Polym. Mater. Polym. Biomater.*, 2022, **71**(3), 180–195.

20 L. Vaiani, A. Boccaccio, A. E. Uva, G. Palumbo, A. Piccininni, P. Guglielmi, S. Cantore, L. Santacroce, I. A. Charitos and A. Ballini, Ceramic materials for biomedical applications: An overview on properties and fabrication processes, *J. Funct. Biomater.*, 2023, **14**(3), 146.

21 L. Wu, F. Feyerabend, A. F. Schilling, R. Willumeit-Römer and B. J. Luthringer, Effects of extracellular magnesium extract on the proliferation and differentiation of human osteoblasts and osteoclasts in coculture, *Acta Biomater.*, 2015, **27**, 294–304.

22 M. Diba, F. Tapia, A. R. Boccaccini and L. A. Strobel, Magnesium-containing bioactive glasses for biomedical applications, *Int. J. Appl. Glass Sci.*, 2012, **3**(3), 221–253.

23 C. Wu and J. Chang, Degradation, bioactivity, and cytocompatibility of diopside, akermanite, and bredigite ceramics, *J. Biomed. Mater. Res., Part B*, 2007, **83**(1), 153–160.

24 C. Wu, Y. Ramaswamy and H. Zreiqat, Porous diopside ($CaMgSi_2O_6$) scaffold: A promising bioactive material for bone tissue engineering, *Acta Biomater.*, 2010, **6**(6), 2237–2245.

25 A. Sobhani and E. Salimi, Low temperature preparation of diopside nanoparticles: in-vitro bioactivity and drug loading evaluation, *Sci. Rep.*, 2023, **13**(1), 16330.

26 Y.-S. Tseng, Y.-H. Su, C.-L. Chen, J. Zhang, C.-K. Wang, D. A. H. Hanaor and W.-F. Chen, Bioceramics in the $CaMgSi_2O_6$–Li_2O system: A glass-ceramic strategy for excellent mechanical strength and enhanced bioactivity by spontaneous elemental redistribution, *Adv. Mater. Interfaces*, 2023, **10**(12), 2202491.

27 Y.-H. Su, C.-T. Pan, Y.-S. Tseng, J. Zhang and W.-F. Chen, Rare earth element cerium substituted Ca–Si–Mg system bioceramics: From mechanism to mechanical and degradation properties, *Ceram. Int.*, 2021, **47**(14), 19414–19423.

28 W.-F. Chen, Y.-S. Tseng, Y.-M. Chang, J. Zhang, Y.-H. Su, Z.-H. Wen, D. A. Henry Hanaor, W.-H. Hsu and C.-T. Pan, Mixed phase bioceramics in the $CaMgSi_2O_6$–MoO_3 system: Mechanical properties and in-vitro bioactivity, *Ceram. Int.*, 2021, **47**(23), 32847–32855.

29 I. Kansal, A. Goel, D. U. Tulyaganov and J. M. F. Ferreira, Effect of some rare-earth oxides on structure, devitrification and properties of diopside based glasses, *Ceram. Int.*, 2009, **35**(8), 3221–3227.

30 R. Titorenkova, V. Kostov-Kytin and T. Dimitrov, Synthesis, phase composition and characterization of Co-diopside ceramic pigments, *Ceram. Int.*, 2022, **48**(24), 36781–36788.

31 P. K. Sadh, S. Duhan and J. S. Duhan, Agro-industrial wastes and their utilization using solid state fermentation: a review, *Bioresour. Bioprocess*, 2018, **5**(1), 1–15.

32 E. Benetto, K. Gericke and M. Guiton, *Designing sustainable technologies, products and policies: from science to innovation*, Springer, Cham, Luxembourg, 2018.

33 FAO, 2023, Agricultural production statistics 2000–2022, FAOSTAT Analytical Briefs, DOI: **10.4060/cc9205en**.

34 D. Oliveira, P. Benelli and E. Amante, A literature review on adding value to solid residues: egg shells, *J. Clean. Prod.*, 2013, **46**, 42–47.

35 M. Baláž, A. Zorkovská, M. Fabián, V. Girman and J. Briančin, Eggshell biomaterial: Characterization of nanophase and

polymorphs after mechanical activation, *Adv. Powder Technol.*, 2015, **26**(6), 1597–1608.
36 E. M. Rivera, M. Araiza, W. Brostow, V. M. Castano, J. Dıaz-Estrada, R. Hernández and J. R. Rodrıguez, Synthesis of hydroxyapatite from eggshells, *Mater. Lett.*, 1999, **41**(3), 128–134.
37 R. Pode, Potential applications of rice husk ash waste from rice husk biomass power plant, *Renewable Sustainable Energy Rev.*, 2016, **53**, 1468–1485.
38 V. P. Della, I. Kühn and D. Hotza, Rice husk ash as an alternate source for active silica production, *Mater. Lett.*, 2002, **57**(4), 818–821.
39 R. A. Bakar, R. Yahya and S. N. Gan, Production of high purity amorphous silica from rice husk, *Procedia Chem.*, 2016, **19**, 189–195.
40 A. Chicheł, J. Skowronek, M. Kubaszewska and M. Kanikowski, Hyperthermia–description of a method and a review of clinical applications, *Rep. Pract. Oncol. Radiother.*, 2007, **12**(5), 267–275.
41 H. B. Simon, Hyperthermia, *N. Engl. J. Med.*, 1993, **329**(7), 483–487.
42 G. Hannon, F. L. Tansi, I. Hilger and A. Prina-Mello, The effects of localized heat on the hallmarks of cancer, *Adv. Ther.*, 2021, **4**(7), 2000267.
43 K. Qi, B. Sun, S.-Y. Liu and M. Zhang, Research progress on carbon materials in tumor photothermal therapy, *Biomed. Pharmacother.*, 2023, **165**, 115070.
44 M. Abdellahi, E. Karamian, A. Najafinezhad, F. Ranjabar, A. Chami and A. Khandan, Diopside-magnetite; A novel nanocomposite for hyperthermia applications, *J. Mech. Behav. Biomed. Mater.*, 2018, **77**, 534–538.
45 I. Sharifi, H. Shokrollahi and S. Amiri, Ferrite-based magnetic nanofluids used in hyperthermia applications, *J. Magn. Magn. Mater.*, 2012, **324**(6), 903–915.
46 N. Tran and T. J. Webster, Magnetic nanoparticles: biomedical applications and challenges, *J. Mater. Chem.*, 2010, **20**(40), 8760–8767.
47 Y. Zhang, D. Zhai, M. Xu, Q. Yao, J. Chang and C. Wu, 3D-printed bioceramic scaffolds with a Fe_3O_4/graphene oxide nanocomposite interface for hyperthermia therapy of bone tumor cells, *J. Mater. Chem. B*, 2016, **4**(17), 2874–2886.
48 M. M. Salmani, M. Hashemian and A. Khandan, Therapeutic effect of magnetic nanoparticles on calcium silicate bioceramic in alternating field for biomedical application, *Ceram. Int.*, 2020, **46**(17), 27299–27307.
49 S. Jadhav, P. Shewale, B. Shin, M. Patil, G. Kim, A. Rokade, S. Park, R. Bohara and Y. Yu, Study of structural and magnetic properties and heat induction of gadolinium-substituted manganese zinc ferrite nanoparticles for *in vitro* magnetic fluid hyperthermia, *J. Colloid Interface Sci.*, 2019, **541**, 192–203.
50 A. Jasemi, B. K. Moghadas, A. Khandan and S. Saber-Samandari, A porous calcium-zirconia scaffolds composed of magnetic nanoparticles for bone cancer treatment: Fabrication, characterization and FEM analysis, *Ceram. Int.*, 2022, **48**(1), 1314–1325.
51 S. R. Patade, D. D. Andhare, S. B. Somvanshi, S. A. Jadhav, M. V. Khedkar and K. Jadhav, Self-heating evaluation of superparamagnetic $MnFe_2O_4$ nanoparticles for magnetic fluid hyperthermia application towards cancer treatment, *Ceram. Int.*, 2020, **46**(16), 25576–25583.
52 N. Thorat, S. Otari, R. Patil, R. Bohara, H. Yadav, V. Koli, A. Chaurasia and R. Ningthoujam, Synthesis, characterization and biocompatibility of chitosan functionalized superparamagnetic nanoparticles for heat activated curing of cancer cells, *Dalton Trans.*, 2014, **43**(46), 17343–17351.
53 K. Sharma and C. Chauhan, Role of magnetic nanoparticle (MNPs) in cancer treatment: a review, *Mater. Today: Proc.*, 2021, **81**, 919–925.
54 R. R. Koli, N. G. Deshpande, D. S. Kim, A. R. Shelke, A. V. Fulari, V. J. Fulari and H. K. Cho, Tailoring the magnetic hyperthermia performances of gram-bean-extract-mediated highly disperse MFe_2O_4 (M = Fe, Ni, Mn) nanoferrites, *Ceram. Int.*, 2020, **46**(15), 24290–24301.
55 A. Makridis, K. Topouridou, M. Tziomaki, D. Sakellari, K. Simeonidis, M. Angelakeris, M. P. Yavropoulou, J. G. Yovos and O. Kalogirou, *In vitro* application of Mn–ferrite nanoparticles as novel magnetic hyperthermia agents, *J. Mater. Chem. B*, 2014, **2**(47), 8390–8398.
56 J. Zhang, S. Zhao, M. Zhu, Y. Zhu, Y. Zhang, Z. Liu and C. Zhang, 3D-printed magnetic Fe_3O_4/MBG/PCL composite scaffolds with multifunctionality of bone regeneration, local anticancer drug delivery and hyperthermia, *J. Mater. Chem. B*, 2014, **2**(43), 7583–7595.
57 S. Zhang, H. Niu, Y. Cai, X. Zhao and Y. Shi, Arsenite and arsenate adsorption on coprecipitated bimetal oxide magnetic nanomaterials: $MnFe_2O_4$ and $CoFe_2O_4$, *Chem. Eng. J.*, 2010, **158**(3), 599–607.
58 R. E. Rosensweig, Heating magnetic fluid with alternating magnetic field, *J. Magn. Magn. Mater.*, 2002, **252**, 370–374.
59 A. E. Deatsch and E. E. Evans, Heating efficiency in magnetic nanoparticle hyperthermia, *J. Magn. Magn. Mater.*, 2014, **354**, 163–172.
60 J. Yuan, Z. Ye, Y. Zeng, Z. Pan, Z. Feng, Y. Bao, Y. Li, X. Liu, Y. He and Q. Feng, Bifunctional scaffolds for tumor therapy and bone regeneration: Synergistic effect and interplay between therapeutic agents and scaffold materials, *Mater. Today Bio*, 2022, **15**, 100318.
61 Z. Yu, H. Wang, B. Ying, X. Mei, D. Zeng, S. Liu, W. Qu, X. Pan, S. Pu, R. Li and Y. Qin, Mild photothermal therapy assist in promoting bone repair: Related mechanism and materials, *Mater. Today Bio*, 2023, **23**, 100834.
62 N. Akhlaghi and G. Najafpour-Darzi, Manganese ferrite ($MnFe_2O_4$) Nanoparticles: From synthesis to application-A review, *J. Ind. Eng. Chem.*, 2021, **103**, 292–304.
63 K. Asghar, M. Qasim and D. Das, Preparation and characterization of mesoporous magnetic $MnFe_2O_4$@$mSiO_2$ nanocomposite for drug delivery application, *Mater. Today: Proc.*, 2020, **26**, 87–93.
64 M. M. Baig, M. A. Yousuf, P. O. Agboola, M. A. Khan, I. Shakir and M. F. Warsi, Optimization of different wet

chemical routes and phase evolution studies of $MnFe_2O_4$ nanoparticles, *Ceram. Int.*, 2019, **45**(10), 12682–12690.

65 H. Shen, Z. Xiang and A. Dang, Enhanced peroxidase-like activity of $MnFe_2O_4$ nanoparticles on halloysite nanotubes for uric acid detection, *Asia-Pac. J. Chem. Eng.*, 2025, **20**(1), e3143.

66 R. V. Chernozem, A. O. Urakova, P. V. Chernozem, D. A. Koptsev, Y. R. Mukhortova, I. Y. Grubova, D. V. Wagner, E. Y. Gerasimov, M. A. Surmeneva, A. L. Kholkin and R. A. Surmenev, Novel biocompatible magnetoelectric $MnFe_2O_4$ Core@BCZT shell nano–hetero-structures with efficient catalytic performance, *Small*, 2023, **19**(42), 2302808.

67 C. R. Kalaiselvan, S. S. Laha, S. B. Somvanshi, T. A. Tabish, N. D. Thorat and N. K. Sahu, Manganese ferrite ($MnFe_2O_4$) nanostructures for cancer theranostics, *Coord. Chem. Rev.*, 2022, **473**, 214809.

68 B. Aslibeiki, P. Kameli and M. H. Ehsani, $MnFe_2O_4$ bulk, nanoparticles and film: A comparative study of structural and magnetic properties, *Ceram. Int.*, 2016, **42**(11), 12789–12795.

69 B. D. Cullity and C. D. Graham, Ferrimagnetism, *Introduction to Magnetic Materials*, 2008, pp. 175–195.

70 S. Jeyaram and R. J. Joseyphus, Enhanced heating efficiency in Mn–Zn ferrite nanoparticles with optimized magnetic anisotropy energy, *J. Phys. Chem. Solids*, 2025, **207**, 112992.

71 S. S. Danewalia and K. Singh, Bioactive glasses and glass-ceramics for hyperthermia treatment of cancer: state-of-art, challenges, and future perspectives, *Mater. Today Bio*, 2021, **10**, 100100.

72 G. Li, S. Feng and D. Zhou, Magnetic bioactive glass ceramic in the system $CaO–P_2O_5–SiO_2–MgO–CaF_2–MnO_2–Fe_2O_3$ for hyperthermia treatment of bone tumor, *J. Mater. Sci.: Mater. Med.*, 2011, **22**(10), 2197.

73 Y. Yu, T. Ding, Y. Xue and J. Sun, Osteoinduction and long-term osseointegration promoted by combined effects of nitrogen and manganese elements in high nitrogen nickel-free stainless steel, *J. Mater. Chem. B*, 2016, **4**(4), 801–812.

74 D.-M. Huang, J.-K. Hsiao, Y.-C. Chen, L.-Y. Chien, M. Yao, Y.-K. Chen, B.-S. Ko, S.-C. Hsu, L.-A. Tai, H.-Y. Cheng, S.-W. Wang, C.-S. Yang and Y.-C. Chen, The promotion of human mesenchymal stem cell proliferation by superparamagnetic iron oxide nanoparticles, *Biomaterials*, 2009, **30**(22), 3645–3651.

75 O. Sedighi, A. Alaghmandfard, M. Montazerian and F. Baino, A critical review of bioceramics for magnetic hyperthermia, *J. Am. Ceram. Soc.*, 2022, **105**(3), 1723–1747.

76 A. Moeini, T. Hassanzadeh Chinijani, A. Malek Khachatourian, M. Vinicius Lia Fook, F. Baino and M. Montazerian, A critical review of bioactive glasses and glass–ceramics in cancer therapy, *Int. J. Appl. Glass Sci.*, 2023, **14**(1), 69–87.

77 H. Tripathi, G. C. Pandey, A. Dubey, S. K. Shaw, N. K. Prasad, S. P. Singh and C. Rath, Superparamagnetic manganese ferrite and strontium bioactive glass nanocomposites: Enhanced biocompatibility and antimicrobial properties for hyperthermia application, *Adv. Eng. Mater.*, 2021, **23**(1), 2000275.

78 P. R. Oskoui and M. Rezvani, The dual role of manganese oxide simultaneously in enhancing bioactivity and magnetic properties of glass ceramics used in cancer treatment, *Mater. Chem. Phys.*, 2024, **322**, 129563.

79 A. Mushtaq, R. Zhao, D. Luo, E. Dempsey, X. Wang, M. Z. Iqbal and X. Kong, Magnetic hydroxyapatite nanocomposites: The advances from synthesis to biomedical applications, *Mater. Des.*, 2021, **197**, 109269.

80 W. Pon-On, S. Meejoo and I. M. Tang, Substitution of manganese and iron into hydroxyapatite: Core/shell nanoparticles, *Mater. Res. Bull.*, 2008, **43**(8–9), 2137–2144.

81 A. Arabzadeh, N. Akhlaghi and G. Najafpour-Darzi, Quercetin loading on mesoporous magnetic $MnFe_2O_4$@ hydroxyapatite core-shell nanoparticles for treating cancer cells, *Adv. Powder Technol.*, 2022, **33**(6), 103609.

82 G. Gergely, F. Wéber, I. Lukács, A. L. Tóth, Z. E. Horváth, J. Mihály and C. Balázsi, Preparation and characterization of hydroxyapatite from eggshell, *Ceram. Int.*, 2010, **36**(2), 803–806.

83 P. Kamalanathan, S. Ramesh, L. Bang, A. Niakan, C. Tan, J. Purbolaksono, H. Chandran and W. Teng, Synthesis and sintering of hydroxyapatite derived from eggshells as a calcium precursor, *Ceram. Int.*, 2014, **40**(10), 16349–16359.

84 S. Palakurthy, *In vitro* evaluation of silver doped wollastonite synthesized from natural waste for biomedical applications, *Ceram. Int.*, 2019, **45**(18), 25044–25051.

85 A. Oki, B. Parveen, S. Hossain, S. Adeniji and H. Donahue, Preparation and *in vitro* bioactivity of zinc containing sol–gel–derived bioglass materials, *J. Biomed. Mater. Res., Part A*, 2004, **69**(2), 216–221.

86 L. Habte, N. Shiferaw, D. Mulatu, T. Thenepalli, R. Chilakala and J. W. Ahn, Synthesis of nano-calcium oxide from waste eggshell by sol-gel method, *Sustainability*, 2019, **11**(11), 3196.

87 N. Y. Iwata, G.-H. Lee, Y. Tokuoka and N. Kawashima, Sintering behavior and apatite formation of diopside prepared by coprecipitation process, *Colloids Surf., B*, 2004, **34**(4), 239–245.

88 T. Nonami, C. Takahashi and J. Yamazaki, Synthesis of diopside by alkoxide method and coating on titanium, *J. Ceram. Soc. Jpn.*, 1995, **103**(1199), 703–708.

89 A. Patterson, The Scherrer formula for X-ray particle size determination, *Phys. Rev.*, 1939, **56**(10), 978.

90 J. Jones and L. Hench, Effect of surfactant concentration and composition on the structure and properties of sol-gel-derived bioactive glass foam scaffolds for tissue engineering, *J. Mater. Sci.*, 2003, **38**, 3783–3790.

91 V. Karageorgiou and D. Kaplan, Porosity of 3D biomaterial scaffolds and osteogenesis, *Biomaterials*, 2005, **26**(27), 5474–5491.

92 J. A. Van Orman and K. L. Crispin, Diffusion in oxides, *Rev. Mineral. Geochem.*, 2010, **72**(1), 757–825.

93 R. D. Shannon and C. T. Prewitt, Effective ionic radii in oxides and fluorides, *Acta Crystallogr., Sect. B*, 1969, **25**(5), 925–946.

94 S. K. Boda, A. A. V, B. Basu and B. Sahoo, Structural and magnetic phase transformations of hydroxyapatite-magnetite composites under inert and ambient sintering atmospheres, *J. Phys. Chem. C*, 2015, **119**(12), 6539–6555.
95 S. Sprio, S. Panseri, A. Adamiano, M. Sandri, M. Uhlarz, T. Herrmannsdörfer, E. Landi, Y. Pineiro-Remondo and A. Tampieri, Porous hydroxyapatite-magnetite composites as carriers for guided bone regeneration, *Front. Nanosci. Nanotechol.*, 2017, **3**(1), 1000145.
96 M. Biesuz, A. Galotta, A. Motta, M. Kermani, S. Grasso, J. Vontorová, V. Tyrpekl, M. Vilémová and V. M. Sglavo, Speedy bioceramics: Rapid densification of tricalcium phosphate by ultrafast high-temperature sintering, *Mater. Sci. Eng., C*, 2021, **127**, 112246.
97 K. Vamvakidis, M. Katsikini, D. Sakellari, E. Paloura, O. Kalogirou and C. Dendrinou-Samara, Reducing the inversion degree of $MnFe_2O_4$ nanoparticles through synthesis to enhance magnetization: evaluation of their ^{1}H NMR relaxation and heating efficiency, *Dalton Trans.*, 2014, **43**(33), 12754–12765.
98 A. Doaga, A. Cojocariu, W. Amin, F. Heib, P. Bender, R. Hempelmann and O. Caltun, Synthesis and characterizations of manganese ferrites for hyperthermia applications, *Mater. Chem. Phys.*, 2013, **143**(1), 305–310.
99 L. H. Nguyen, N. X. Phuc, D. H. Manh, N. H. Nam, N. X. Truong, N. V. Quynh, P. T. Phong and P. H. Nam, Size-dependent magnetic heating of $MnFe_2O_4$ nanoparticles, *J. Electron. Mater.*, 2021, **50**(9), 5318–5326.
100 Y. Ma, X. Xu, L. Lu, K. Meng, Y. Wu, J. Chen, J. Miao and Y. Jiang, Facile synthesis of ultrasmall $MnFe_2O_4$ nanoparticles with high saturation magnetization for magnetic resonance imaging, *Ceram. Int.*, 2021, **47**(24), 34005–34011.
101 M. S. Nunes, M. A. Morales, A. Paesano and J. H. de Araújo, Synthesis and characterization of monophasic $MnFe_2O_4$ nanoparticles for potential application in magnetic hyperthermia, *Ceram. Int.*, 2024, **50**(14), 25333–25341.
102 C. Iacovita, A. Florea, L. Scorus, E. Pall, R. Dudric, A. I. Moldovan, R. Stiufiuc, R. Tetean and C. M. Lucaciu, Hyperthermia, cytotoxicity, and cellular uptake properties of manganese and zinc ferrite magnetic nanoparticles synthesized by a polyol-mediated process, *Nanomaterials*, 2019, **9**(10), 1489.
103 B. Issa, I. M. Obaidat, B. A. Albiss and Y. Haik, Magnetic nanoparticles: surface effects and properties related to biomedicine applications, *Int. J. Mol. Sci.*, 2013, **14**(11), 21266–21305.
104 S.-h Noh, W. Na, J.-t Jang, J.-H. Lee, E. J. Lee, S. H. Moon, Y. Lim, J.-S. Shin and J. Cheon, Nanoscale magnetism control *via* surface and exchange anisotropy for optimized ferrimagnetic hysteresis, *Nano Lett.*, 2012, **12**(7), 3716–3721.
105 R. Hergt and S. Dutz, Magnetic particle hyperthermia—biophysical limitations of a visionary tumour therapy, *J. Magn. Magn. Mater.*, 2007, **311**(1), 187–192.
106 I. A. Brezovich, Low frequency hyperthermia: capacitive and ferromagnetic thermoseed methods, *Med. Phys. Monogr.*, 1988, **16**, 82–111.
107 C. L. Frewin, M. Nezafati, K. Noble and S. E. Saddow, Cytotoxicity of 3C–SiC investigated through strict adherence to ISO 10993, *Silicon Carbide Biotechnology*, Elsevier, 2016, pp. 27–61.
108 S. Pang, D. Wu, F. Kamutzki, J. Kurreck, A. Gurlo and D. A. Hanaor, High performing additively manufactured bone scaffolds based on copper substituted diopside, *Mater. Des.*, 2022, **215**, 110480.
109 T. A. Owen, M. Aronow, V. Shalhoub, L. M. Barone, L. Wilming, M. S. Tassinari, M. B. Kennedy, S. Pockwinse, J. B. Lian and G. S. Stein, Progressive development of the rat osteoblast phenotype *in vitro*: reciprocal relationships in expression of genes associated with osteoblast proliferation and differentiation during formation of the bone extracellular matrix, *J. Cell. Physiol.*, 1990, **143**(3), 420–430.
110 L.-s Chen, M. Zhang, P. Chen, X.-f Xiong, P.-q Liu, H.-b Wang, J.-j Wang and J. Shen, The m6A demethylase FTO promotes the osteogenesis of mesenchymal stem cells by downregulating PPARG, *Acta Pharmacol. Sin.*, 2022, **43**(5), 1311–1323.
111 O. Tsigkou, J. R. Jones, J. M. Polak and M. M. Stevens, Differentiation of fetal osteoblasts and formation of mineralized bone nodules by 45S5 Bioglass® conditioned medium in the absence of osteogenic supplements, *Biomaterials*, 2009, **30**(21), 3542–3550.
112 S. Yeniyol and J. L. Ricci, Alkaline phosphatase levels of murine pre-osteoblastic cells on anodized and annealed titanium surfaces, *Eur. Oral Res.*, 2018, **52**(1), 12–18.
113 Y. Wu, W. Jiang, X. Wen, B. He, X. Zeng, G. Wang and Z. Gu, A novel calcium phosphate ceramic–magnetic nanoparticle composite as a potential bone substitute, *Biomed. Mater.*, 2010, **5**(1), 015001.
114 J. Li, C. Deng, W. Liang, F. Kang, Y. Bai, B. Ma, C. Wu and S. Dong, Mn-containing bioceramics inhibit osteoclastogenesis and promote osteoporotic bone regeneration *via* scavenging ROS, *Bioact. Mater.*, 2021, **6**(11), 3839–3850.
115 R. Staruch, R. Chopra and K. Hynynen, Hyperthermia in bone generated with MR imaging-controlled focused ultrasound: Control strategies and drug delivery, *Radiology*, 2012, **263**(1), 117–127.
116 L. Wang, P. Hu, H. Jiang, J. Zhao, J. Tang, D. Jiang, J. Wang, J. Shi and W. Jia, Mild hyperthermia-mediated osteogenesis and angiogenesis play a critical role in magnetothermal composite-induced bone regeneration, *Nano Today*, 2022, **43**, 101401.
117 F. De Tommasi, C. Massaroni, R. F. Grasso, M. Carassiti and E. Schena, Temperature monitoring in hyperthermia treatments of bone tumors: State-of-the-art and future challenges, *Sensors*, 2021, **21**(16), 5470.